



# **MAGNETIC DATA MODELING APPLIED TO A ZONE WITH EMERALD POTENTIAL IN BOYACÁ, COLOMBIA**

Carol Vanessa Barrera López

University of los Andes  
Science Faculty, Geosciences Department  
Bogotá, Colombia  
2018

# **MAGNETIC DATA MODELING APPLIED TO A ZONE WITH EMERALD POTENTIAL IN BOYACÁ, COLOMBIA**

Carol Vanessa Barrera López

In partial fulfillment of the requirements for the degree of:  
**Geoscientist**

Director:  
Ph.D. in Marine Geophysics and Master in Geophysics Jean Baptiste Tary

Line of Research:  
Exploration Geophysics

University of los Andes  
Science Faculty, Geosciences Department  
Bogotá, Colombia  
2018

## **Acknowledgments**

Special thanks to Jose Ernesto Cardenas Santamaría, legal representative of SIGMIN SAS, and his work team for providing all the field work costs and the area for applying the method. Also thanks to Felipe Arrubla Arango for being the contact to Jose and helping in the geophysical survey, to Juan Sebastian Barbosa, Andres Felipe Escobar and all my friends who helped me in the development of the document. Finally special thanks to Jean Baptiste Tary for giving me the knowledge and support me in the development of this project.

## RESUMEN

Se desarrolla un modelo de datos magnéticos en una zona con potencial para depósitos de esmeralda en Boyacá, Colombia. Para lograr este objetivo, se sigue un plan de modelamiento de dos pasos. El primero es un modelo continuo (*Forward model*), que utiliza prismas rectangulares para representar el subsuelo y nos permite predecir la anomalía magnética en la inferencia de un depósito mineral. La segunda es la inversión de los datos, desarrollada usando el software ZondGM2D, que implementa una solución de mínimos cuadrados ponderados amortiguados a través del método Occam. Con el primer paso se obtuvo la respuesta teórica de un modelo propuesto de mineralización en el área de estudio. Para aplicar el segundo paso, el software ZondGM2D se probó con datos sintéticos, lo cual mostró la precisión de los algoritmos en términos de ubicación de la fuente de la anomalía. Finalmente, los modelos de susceptibilidad magnéticas 2D obtenidos por la inversión posiblemente muestran la falla de Itoco que está relacionada con los depósitos de esmeralda de la zona.

**Palabras clave:** *Forward model*, Inversión, depósitos de esmeralda, Susceptibilidad magnética, ZondGM2D.

## ABSTRACT

A magnetic data model is developed in a zone with potential for emerald deposits in Boyacá, Colombia. In order to achieve this objective, a two-step modelling plan is followed. The first one is a forward model, which uses rectangular prism cells to represent the subsurface and let us predict the magnetic anomaly in the inference of a mineral deposit. The second one is the inversion of the data, developed using the ZondGM2D software which implements a weighted damped least squares solution through the Occam method. From the first step, the theoretical response of a proposed model of the mineralization in the place was obtained. In order to apply the second step, the ZondGM2D software was tested with synthetic data, showing the accuracy of the algorithms in terms of locating the anomaly source. Finally, the 2D magnetic susceptibility models obtained by the inversion possibly show the Itoco fault which is related with the emerald deposits of the zone.

**Key words:** Forward model, Inversion, emeral deposits, Magnetic susceptibility, ZondGM2D.

# TABLE OF CONTENTS

RESUMEN .....	IV
ABSTRACT .....	V
Introduction .....	1
1. Study Area .....	3
1.1 Geological Background .....	4
1.1.1 Stratigraphy .....	4
1.2 Tectonic Background .....	5
1.3 Mineralization .....	6
2. Methodology .....	8
2.1 Magnetic Method .....	8
2.2 Magnetometer .....	9
2.2.1 Optically Pumped Magnetometer .....	10
2.3 Processing of the magnetic field measurements .....	11
2.4 Magnetic anomaly modelling .....	12
2.4.1 Forward Modelling .....	12
2.4.2 Inversion .....	14
3. Data Acquisition .....	17
4. Results .....	19
4.1 Benchmark of the code .....	19
4.2 Synthetic example .....	22
4.3 Synthetic data inversion .....	25
4.4 Real data inversion .....	26
4.4.1 ZondGM2D Results .....	27
5. Discussion .....	30
5.1 Geological interpretation of the models .....	31
6. Conclusions .....	33

## FIGURE AND TABLE INDEX

<b>Figure 1.</b> Simplified geological map of the Eastern Cordillera Basin in Colombia (Pignatelly, 2015).....	2
<b>Figure 2.</b> Geographic localization of the study area.....	3
<b>Figure 3.</b> Eastern Cordillera principal boundaries and faults (Taken from Cooper et al., 1995). ....	4
<b>Figure 4.</b> Geological map of study area (The polygon) situated between Muzo and Quípama. ....	6
<b>Figure 5.</b> Cross section of the Tequendama Mine (3km at the west of the study area along the Itoco brook). ....	7
<b>Figure 6.</b> Principle of operation of the optically pumped magnetometer (Lowrie, 2007). ....	10
<b>Figure 7.</b> Rectangular prism (Taken from Liu et al., 2013). ....	13
<b>Figure 8.</b> Aerial photography of the study area with the Profiles of magnetic data and the position of the base station as a red triangle. It is clear that the profiles were taken in the most suitable area within the mining title (taken from Google Earth).....	18
<b>Figure 9.</b> Anomaly of a finite dipole with different inclinations. The one with the continuous line represent the anomaly with an inclination of $90^\circ$ and at the right is the explanation given by (Lowrie, 2007). The model have a susceptibility of $k = 3 \times 10^{-3}$ SI, $M = 31000$ nT and $A_0 = 0^\circ$ . The inclination tested values were $I_0 = 90^\circ, 60^\circ, 45^\circ, 15^\circ$ and $0^\circ$ . ....	19
<b>Figure 10.</b> Comparison of the shape of the anomaly of a vertically magnetized ( $I_0 = 90^\circ$ ) crustal block in which <b>a)</b> $m/z_1 = 1$ , <b>b)</b> $m/z_1 = 2$ and <b>c)</b> $m/z_1 = 8$ . It can be seen that the block widens with respect to its depth, its amplitude decreases and the negative lobes grow. At the left side is the model followed by Lowrie (2007) to calculate the anomaly (modified from Lowrie, 2007). ....	20
<b>Figure 11.</b> Profiles for a dipping sheet for $I_0 = 60^\circ, A_0 = 45^\circ, \text{Dip} = 45^\circ, b = 2d, D = 3.5d$ (with $d = 12$ m, $M = 30000$ nT and $k = 3 \times 10^{-3}$ SI in the model) (modified from Telford et al., 1990) where <b>a)</b> is the response of the code, <b>b)</b> is the example presented by Telford et al. (1990) and <b>c)</b> is the response of the modified code.....	21
<b>Figure 12. a)</b> Breccia of calcite of approximately 2.5 m. It is modeled as a dipping sheet because of the structural geology of the zone. Dip angle of $45^\circ$ and the magnetic field parameters are the ones mentioned in <b>Table 2. b)</b> A model with only the magnetic susceptibility of the black shale which is the background of (a).....	23
<b>Figure 13.</b> Model of the mineralization of the zone. The top of the biggest breccia is at 30 m and is dipping with an angle of $45^\circ$ . The magnetic field parameters are the ones mentioned in <b>Table 2.</b> .....	25

**Figure 14.** Synthetic data and the model of magnetic susceptibilities (where the dipping sheet has a magnetic susceptibility of  $k = -0.008 \times 10^{-3}$ (SI) and the background a  $k = 0.6 \times 10^{-3}$ (SI)). The model is divided in 40 by 80 prisms and the magnetic field parameters are the ones mentioned in **Table 2**. .....26

**Figure 15.** 2D magnetic susceptibility model generated with damped least squares inversion method for the profile 1 (with a rms error of 0.6 nT).  $I_0 = 29.2142^\circ$  and  $D_0 = -7.4913^\circ$  .....27

**Figure 16.** Results of the inversion of the synthetic data with the Occam method using the software ZondGM2D with parameter values of  $I_0 = 29.2142^\circ$  and  $D_0 = -7.4913^\circ$ . The magnetic susceptibility contrasts are in  $10^{-5}$ CGS units. The contour demark the shape of the proposed body. (Rms error of 0.0012). .....28

**Figure 17.** 2D Model of Magnetic susceptibilities for Profile 1 (azimuth  $A = -3.8^\circ$ ). Rms error of 0.065. Dashed red line represent the estimated values. The values of  $\Delta\chi_m$  vary between  $-0.02 \times 10^{-5}$  (CGS) and  $0.8 \times 10^{-5}$  (CGS). .....29

**Figure 18.** 2D Model of Magnetic susceptibilities for Profile 2 (azimuth  $A = -122^\circ$ ). Rms error of 0.51. Dashed red line represent the estimated values. The values of  $\Delta\chi_m$  vary between  $-0.5 \times 10^{-5}$  (CGS) and  $2.5 \times 10^{-5}$  (CGS). .....30

**Figure 19.** Geological interpretation of the 2D models of magnetic susceptibilities for a) Profile 1 and b) Profile 2. ....32

**Table 1.** Magnetic susceptibilities of the model (Telford, Geldart & Sheriff, 1990, p. 74). .....22

**Table 2.** Induced magnetic field parameter values over the study area in the date of the data acquisition (Taken from the International Geomagnetic Reference Field (IGRF-12)). ..... 22

## Introduction

The emerald deposits in Colombia are hosted by Lower Cretaceous sedimentary rocks in the Eastern Cordillera Basin forming two mineralized belts located on the Eastern side (with the mining districts of Gachalá, Chivor, and Macanal) and western border of the basin (with La Glorieta-Yacopi, Muzo, Coscuez, La Pita, and Peñas Blancas mining districts) (**Figure 1**) (Pignatelly et al. 2015). The deposits on the western side are contained in black shales and intercalated dolomitic limestones of Valanginian-Hauterivian age (130-116 Ma) corresponding to the Rosablanca and Paja formations. They are formed as the consequence of a compressive phase characterized by folding and thrusting along tear faults (Pignatelly et al., 2015).

These deposits are unusual because they are described with a hydrothermal model controlled by tectonic structures instead of a magmatic event as most of the emerald deposits in the world (Groat et al., 2008). The emerald is a variety of beryl that is green due to *Al* being replaced in the crystal structure by trace amounts of *Cr* and/or *V* (Groat et al., 2008). The model consists of hot briny fluids (*NaCl*-saturated) that circulated along thrust-fault propagation and interacted with black shales. That interaction lead to the thermal reduction of evaporitic sulfate ions ( $SO_4^{2-}$ ) by organic matter in black shale to form other chemical components as hydrogen sulfide ( $H_2S$ ) and bicarbonate ( $HCO_3^-$ ). The products generated by this process, at 300°C, released from the black shale the elements that enabled emerald formation which are chromium, vanadium, and beryllium (Pignatelly et al., 2015).

In this thesis project, I apply a magnetic method in order to study the emerald mineralization at depth in an area in the Western emerald belt of the Eastern Cordillera in Boyacá, Colombia. In the study area, no geophysical studies have been carried out previously and the localization and size of the emerald mineralization is not accurately defined. I chose this geophysical method as it is relatively inexpensive and is widely used for the direct detection of several different types of mineral deposits and for pseudo-geological mapping (Dentith & Mudge, 2014). This method works with the fact that the magnetic field that is measured at any location is a combination of the Earth's magnetic field plus effects from nearby objects with induced (or remnant) magnetization that are

controlled by a physical property called magnetic susceptibility (Cook, 1997; Dentith & Mudge, 2014).

The aim of this thesis project is to interpret the magnetic anomalies in the study area through the use of 2 D models of magnetic susceptibilities that will be generated with the inversion of the magnetic data. This magnetic modelling is directly associated with the mineralogy and structural geology setting at depth which in turn enables the characterization and definition of the potential emerald deposits.

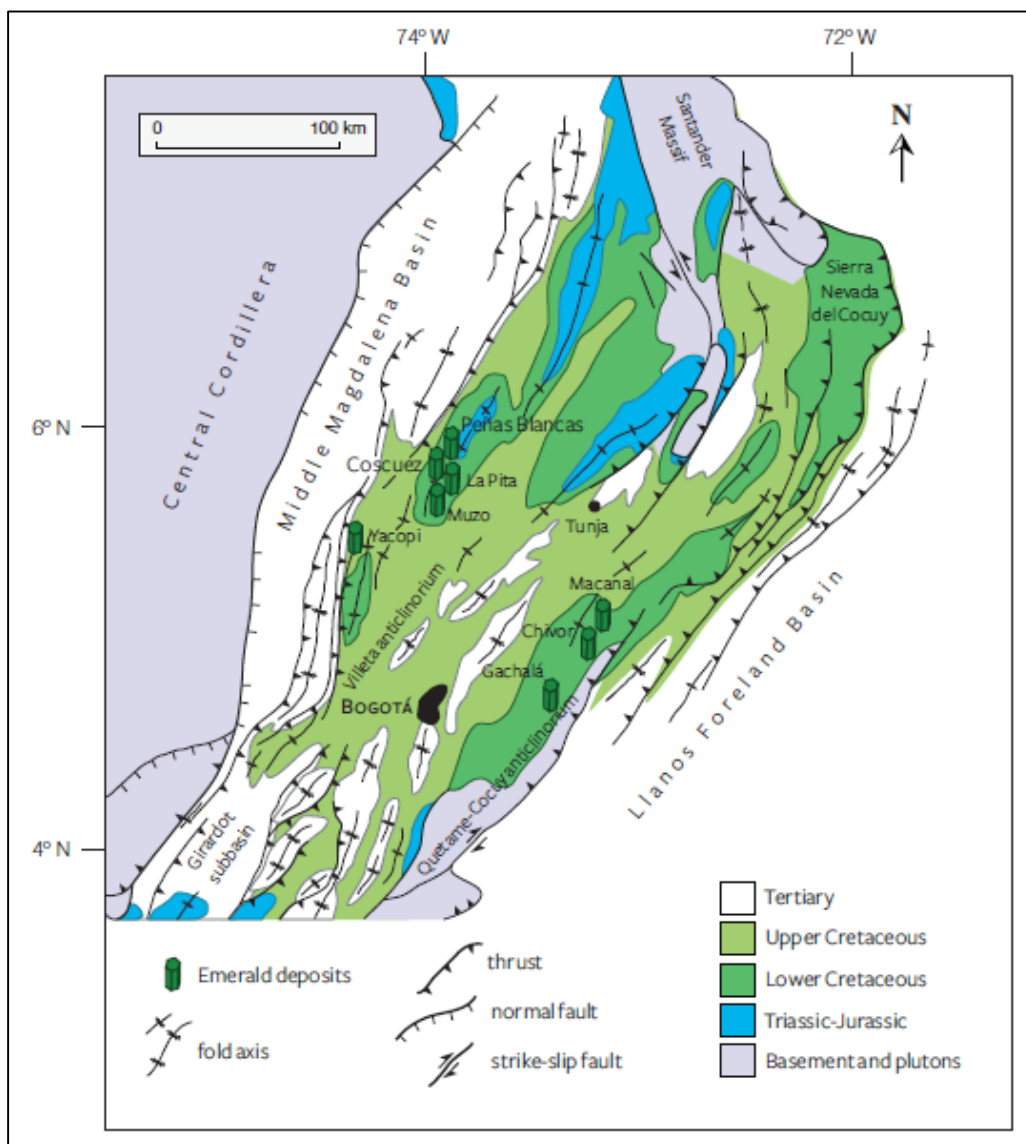


**Figure 1.** Simplified geological map of the Eastern Cordillera Basin in Colombia (Taken from Pignatelly et al., 2015).

## 1. Study Area

The study area is located within the municipality of Quípama, in the western province of the department of Boyacá, Colombia (**Figure 2**). This zone corresponds to the western emerald belt which extends along the west of Boyacá, Cundinamarca and Santander Departments (Reyes et al., 2006) on the western flank of the Eastern Cordillera. This emerald belt is characterized by the presence of the mining districts La Glorieta-Yacopi, Muzo, Coscuez, La Pita and Peñas Blancas (Pignatelly et al., 2015) (**Figure 1**).

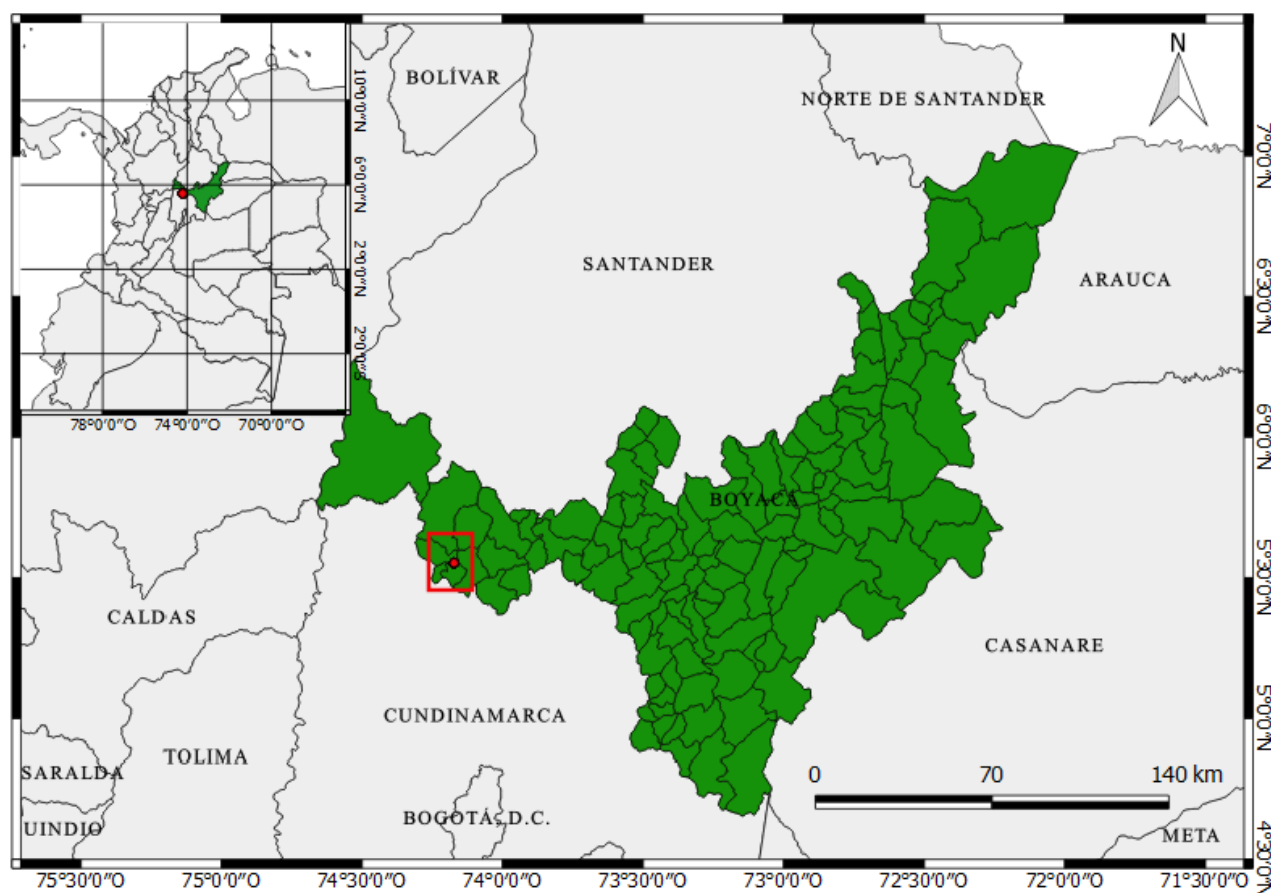


*Figure 2. Geographic localization of the study area.*

## 1.1 Geological Background

The Colombian Andes can be divided into three principal geologic provinces, northeast-southwest- oriented (Parra et al., 2009). The emerald deposits are found in the eastern cordillera (the central province of the Colombian Andes) and is described as a “polyphase-deformed orogenic belt” (Bayona et al., 2008). This cordillera is bounded at the west by the Magdalena river valley, at the east by the Amazonía, the Orinoquía and the Maracaibo lake basin and at the NNE ends with the Oca fault (Guajira Peninsula) (Maya, Buenaventura & Salinas, 2004). (**Figure 3**).

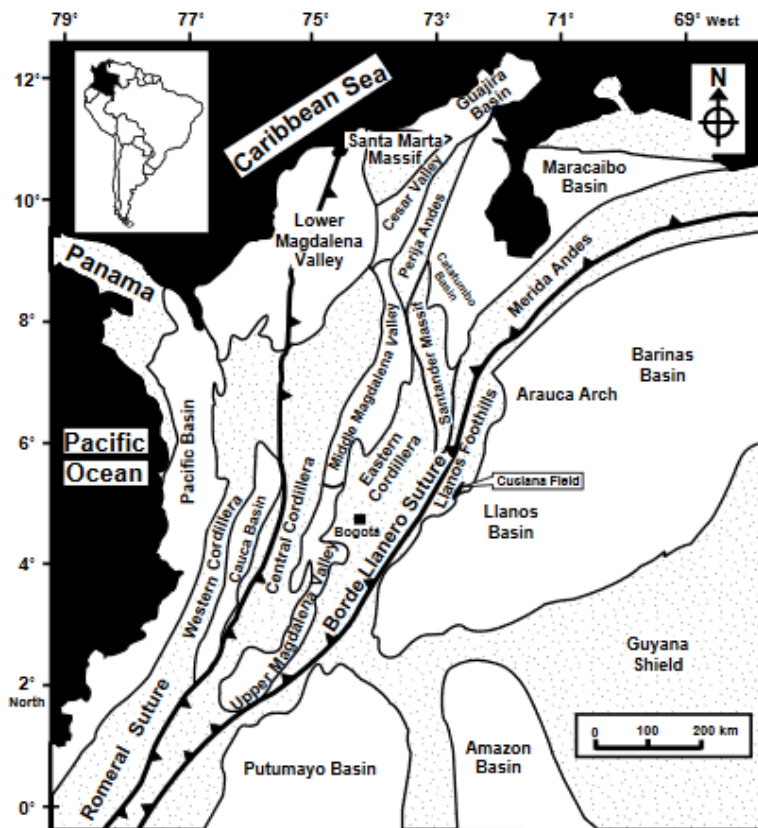


*Figure 3. Eastern Cordillera principal boundaries and faults (Taken from Cooper et al., 1995).*

### 1.1.1 Stratigraphy

It is necessary to know the characteristics of the geological formations in the area in order to generate and obtain a feasible model. As it can be seen in the geological map of the study area (**Figure 4**), the four relevant geological formations for the emerald exploration in the study area

from base to top are the Muzo formation (Hauterivian – Barremian), Capotes formation (Late Aptian – Early Albian), Hilo formation (Medium Albian) and Pacho formation (Upper Albian).

The Muzo formation (also known as Paja formation) is represented by calcareous mudstones intercalated with sandstones and micritic limestones outcropping as part of the flanks of the La Chapa-Borbur Anticline (Reyes et al., 2006). The Capotes formation is described as an intercalation of calcareous shales and loams that turn more silicic at the top around the concordant limit with Hilo formation (Reyes et al., 2006). The Hilo formation is constituted by shales with various packages of silicic siltstones and the Pacho formation is a folded sequence of siltstone, claystone and quartz sandstones (Reyes et al., 2006).

## 1.2 Tectonic Background

The tectonic history of the Eastern Cordillera is characterized by the changes of stress regimes that the western boundary of the South American plate underwent. From the Triassic to the early Cretaceous it was governed by an extensional regime related to a back-arc stretching which was inverted in the Late Cretaceous – early Paleocene to a compressional regime as the Western Cordillera was accreted (Cooper et al., 1995).

The geological structures that define the tectonic setting of the western emerald belt follow the regional tectonic frame mentioned before, which is characterized by having a NNE-SSW direction as well as the direction of the Eastern Cordillera (Maya, Buenaventura & Salinas, 2004). This is the case of the Peñas Blancas Fault (**Figure 4**), a thrust fault with a direction of N20°E that ends at the south by the Itoco fault (Reyes et al., 2006). The Itoco fault is a transverse fault (N50°W) that goes along the Itoco brook bounding the mining zones of Muzo and Las Pavas with a sinistral movement but it also place the north block (Muzo formation) over the south block (Capotes formation) (Reyes et al., 2006)

The principal fold next to the study area is the Coscuéz syncline (Figure 4). It has an orientation that varies from NS to N45°S, an amplitude of 3 km and a longitude of 8 km and is symmetric (Reyes et al., 2006). It is important to take into account the geological structures of the study area in order to estimate a more suitable and credible model of magnetic susceptibilities to describe the

emerald mineralization. An example is the cross-section of the Tequendama mine (at the east of the study area) (**Figure 5**); it allowed the estimation of the most plausible orientation and shape of the mineral deposit in order to apply these parameters to the forward model.

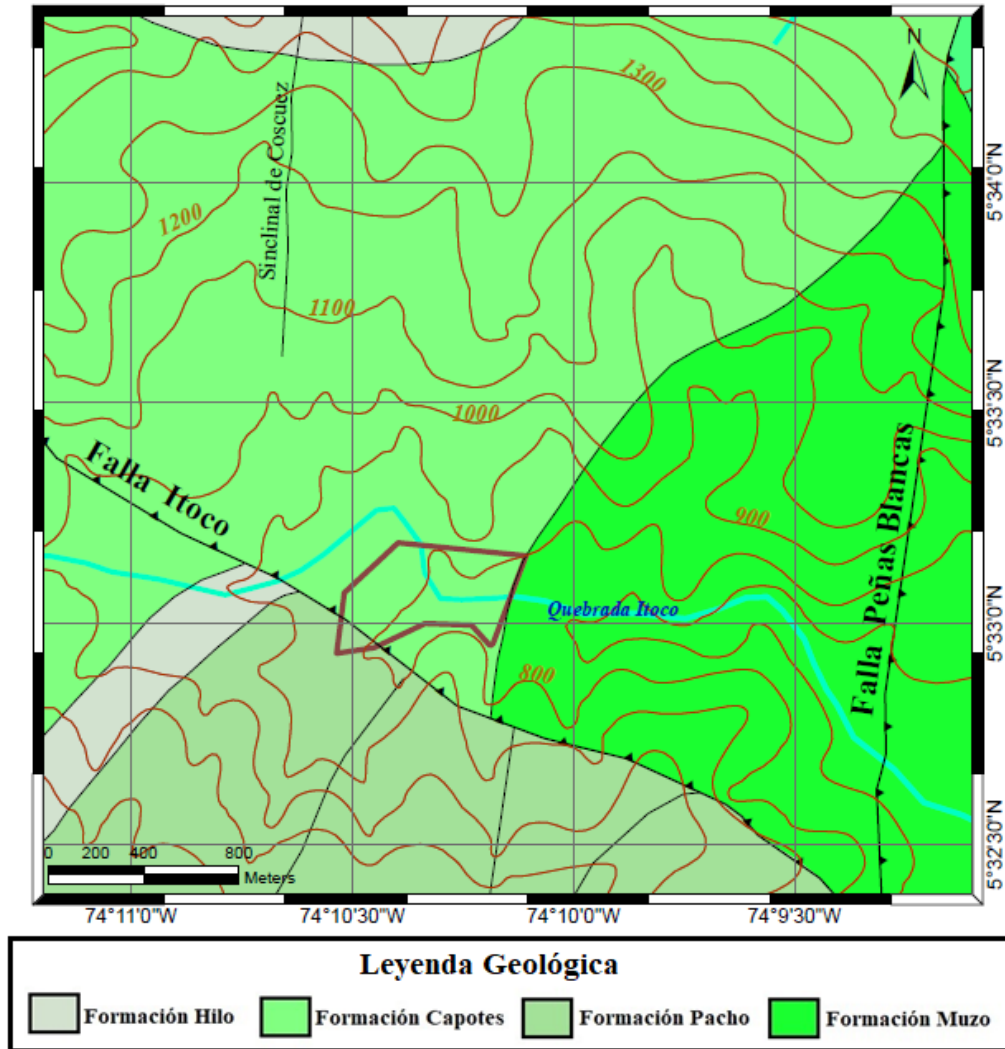


*Figure 4. Geological map of study area (the polygon) situated between Muzo and Quípama.*

### 1.3 Mineralization

The sedimentary rocks in which the emerald deposits are hosted in the Muzo-Quípama mining district from bottom to top are the Valaginian dolomitic limestones from the Rosablanca formation

and the calcareous and siliceous white mudstones and black shales from the Muzo formation (Maya, Buenaventura & Salinas, 2004; Pignatelly et al., 2015; Branquet et al., 1999).

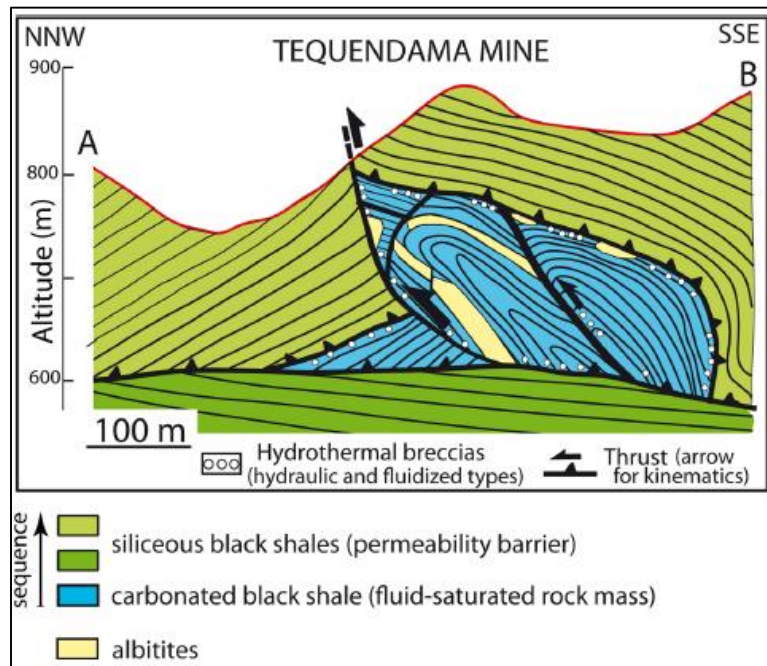


**Figure 5.** Cross section of the Tequendama Mine (3km at the west of the study area along the Itoco brook). “The deposit is linked to tear faults and associated thrusts which are marked by the siliceous black shales overlain by the carbonated ones. The thrust planes are underlain by a hydrothermal breccia (called “cenicero” by the miners) and hydraulic fracturing. The fluid circulation induced intense albitization, carbonization and pyritization of the surrounding black shales (modified from Branquet et al. 1999b)” (Taken from Giuliani et al., 2017).

Field and geochemical studies have led to the development of a hydrothermal genetic model for the emerald deposits in which the parent fluids of the mineralization are hot basinal brines (Branquet et al., 1999) that circulated in a synchronous way to the formation of tear faults and associated thrusts during a compressive tectonic event (Giuliani et al., 2017). Two stages can divide this hydrothermal-sedimentary model proposed by Cheilletz & Giuliani (1996) (Branquet et al., 1999). The stage 1 is characterized by the formation of bedding-parallel veins filled with either fibrous calcite or fibrous pyrite and the albitization of black shales by a three-phase metasomatic fluid (three-phase as it is composed of 75 vol% aqueous brine, 10 vol% of vapour bubble, and 15 vol% of halite daughter mineral) (Branquet et al., 1999; Pignatelly et al., 2015). Stage 2 consists of the development of extensional veins and hydraulic breccia filled with quartz, pyrite, carbonate rhombs, albite and occasionally emerald (Branquet et al., 1999; Groat et al., 2008).

The chemical reactions that accompanied the stages mentioned above can be described as a redox reaction of sulfate ions ( $SO_4^{2-}$ ) that are present in minerals of evaporitic origin with organic

molecules and a carbonic hydrate. This reaction produces large amounts of hydrogen sulfide ( $H_2S$ ) and bicarbonate ( $HCO_3^-$ ) that reacts with calcium ( $Ca^{+2}$ ) and iron ( $Fe^{+2}$ ) released from the black shale by the hydrothermal fluid. That last chemical reaction is responsible for the formation of calcite and pyrite (Groat et al., 2008).

As a result of the described processes, the occurrence of the emerald deposits is in veins of calcite and hydrothermal breccia called by the local miners “cenicero” (ashtray) (Giuliani et al., 2017; Maya, Buenaventura & Salinas, 2004). “The breccia forms non-continuous stratiform bodies which can be traced for up to 50 m along-strike, ranging from 10cm to 3 m thick” (Branquet et al., 1999). The dominant mineralogy is Calcite-Dolomite-Albite (Maya, Buenaventura & Salinas, 2004). More detailed studies done by Romero (1993) define more specific mineral sequences as: quartz-albite, calcite-pyrite-apatite-rutile-coal-pyrite-albite, REE carbonates-dolomite-pyrite-fluorite-calcite (Jimenez, 2017).

## 2. Methodology

### 2.1 Magnetic Method

The magnetic method is a geophysical prospecting technique and as the magnetic field variations are often diagnostic of mineral structures as well as regional structures, it is used for direct detection of several different types of mineral deposits and for pseudo-geological mapping (Dentith & Mudge, 2014; Telford, Geldart, & Sheriff, 1990). This method uses the fact that the magnetic field measured at any location is a combination of the Earth's magnetic field plus effects from nearby objects with induced (or remnant) magnetization (Cook, 1997).

The principle of this method relies in the use of a potential field which is the magnetic field ( $H$  - with SI units of amperes per meter). Following the Ampere's, or also known as Biot-Savart law,  $H$  is a consequence of the flow of an electrical current. If a magnetizable body is placed inside this field it becomes magnetized by induction (that is the lineup of the internal dipoles in the body, also known as magnetization) which produces a field  $M$  (magnetic polarization – SI unit of ampere per meter) that is added to the magnetizing field within the body (Telford, Geldart, & Sheriff, 1990).

The degree to which a body is magnetized is determined by its magnetic susceptibility  $k$ , which is defined by

$$M = kH \quad (1)$$

Magnetic susceptibility is the significant variable in magnetics and is the fundamental rock parameter in magnetic prospecting. The magnetic response of rocks and minerals is determined by the amounts of magnetic moments in them (Telford, Geldart, & Sheriff, 1990). It plays the same role as density does in gravity interpretation and depends upon the magnetic permeability of the material ( $\mu$  - how easily a magnetic field can exist within a material) in the following way (Telford, Geldart, & Sheriff, 1990; Dentith & Mudge, 2014):

$$k = \frac{\mu - \mu_0}{\mu_0} = \frac{\mu}{\mu_0} - 1 \quad (2)$$

Where  $\mu_0$  is the magnetic permeability of a vacuum (with a value of  $4\pi \times 10^{-7}$  henry/m).

The magnetic induction  $B$  (SI unit in Tesla) is the total field, including the effect of magnetization. It can be written

$$B = \mu(H + M) = \mu(1 + k)M \quad (3)$$

When  $H$  and  $M$  are in the same direction, as is usually the case (and then the body is said to be uniformly magnetized). The unit of magnetic induction generally used for geophysical work is the nanotesla ( $nT$ ) (Telford, Geldart, & Sheriff, 1990). “The objective of a geophysical magnetic survey is to render a feasible subsurface distribution of susceptibility that may have given rise to the anomalous fields in the survey data.” (Lelièvre, 2003).

## 2.2 Magnetometer

The magnetometer is the instrument used to measure magnetics fields. Currently, the most important magnetometers (flux-gate, proton-precession and optically pumped) are robust electronic instruments with a high sensitivity (Telford, Geldart, & Sheriff, 1990). The optically pumped magnetometer will be described as it was the one used in the geophysical survey.

### 2.2.1 Optically Pumped Magnetometer

The principle of operation of this type of magnetometer is related to the atomic electrons and the energy levels that they occupy, so it is necessary to select atoms that have magnetic energy sublevels that are suitably spaced to give a measurement of the weak magnetic field of the Earth (in the case of the magnetometers used in this survey, caesium) (Telford, Geldart, & Sheriff, 1990).

Under normal conditions of pressure and temperature, the atoms occupy ground state levels with a known energy difference in between them ( $\sim 10^{-8}$  electron Volt ( $eV$ )) (**Figure 6.a**). If we irradiate a sample with a polarized beam, the atoms will accumulate in one energy level (this technique is known as optical pumping) and as less energy is absorbed the sample becomes increasingly transparent to the irradiating beam (then it reach a maximum current) (**Figure 6.b**). If now we apply an RF (Radio Frequency) signal, with energy corresponding to the transition between the ground state levels, the pumping effect is nullified and the transparency drops to a minimum again (Telford, Geldart, & Sheriff, 1990) (**Figure 6.c**).

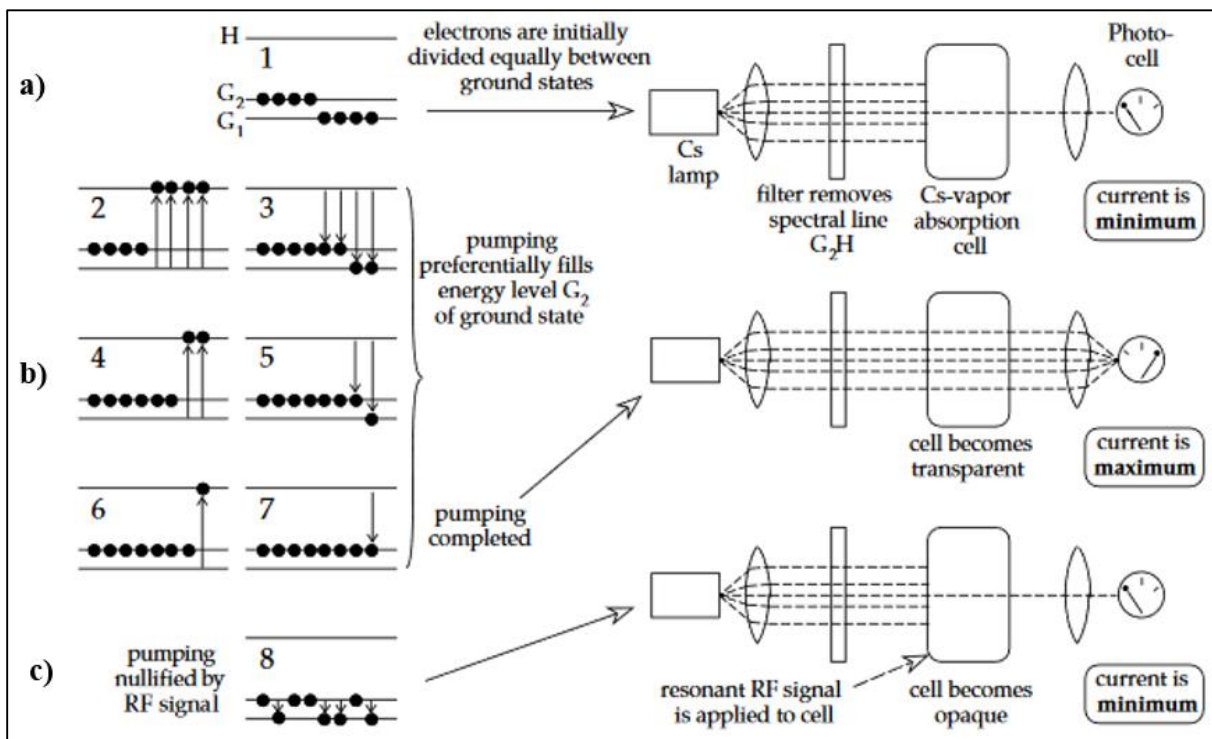


**Figure 6.** Principle of operation of the optically pumped magnetometer (Lowrie, 2007).

The axis of the beam is not aligned with the Earth's field, which causes the electrons to precess about the axis of the field at a frequency known as the Larmor precessional frequency ( $\nu$ ). This precessional frequency consists of a two-part cycle in which an electron spin varies from being almost parallel to almost antiparallel to the field direction which in turn produces a variable light intensity that flickers. Knowing this frequency, and using ( $F = \frac{2\pi\nu}{\gamma_e}$ ), where  $\gamma_e$  is the gyromagnetic ratio of the electron, the total magnetic intensity ( $F$ ) can be calculated. "As the gyromagnetic ratio of the electron is known to a precision of about 1 part in  $10^7$  and because of the relatively high frequencies involved, it is not difficult to measure magnetic field variations as small as  $0.01 \text{ nT}$  with a magnetometer of this type" (Telford, Geldart, & Sheriff, 1990).

### 2.3 Processing of the magnetic field measurements

The magnetic survey data require some corrections in order to guarantee a correct interpretation. The most important effect to compensate is the variation that occurs at the Earth's surface during the course of the day in the intensity of the geomagnetic field, also known as *Diurnal variation* (Lowrie, 2007). This variation is due to the ionosphere component of the Earth's magnetic field and it is controlled by installing within the survey area a fixed base station with a constantly recording magnetometer. The correction is made by removing the control record from the corresponding survey data measurement at a known time (Lowrie, 2007).

The vertical and horizontal variations of the dipole field dominate the variations of the magnetic field with altitude (vertical gradient of the magnetic field), latitude (north-south horizontal gradient of the magnetic field) and longitude. As these corrections have small values on a small-scale survey and also in the geographic zone of the study area (near the equator) it is irrelevant (Lowrie, 2007). The diurnal correction is done using the magnetometer processing software Magmap. With this tool it is also possible to make other corrections to the survey data as remove drop-outs (zero readings), which are effects generated near dead zones or near large ferrous mass, and remove spikes (anomalous readings).

## 2.4 Magnetic anomaly modelling

The interpretation of the magnetic data follows two main steps which are: 1) The calculation of the direct problem (forward modeling) in 2D which is a process of computing data values ( $d$ ) given a model with specific parameters ( $m$ ) and using the mathematical description of a physical law ( $G$ ) (Sacchi, 2006; Snieder & Trampert, 1999); and 2) Solution of the inverse problem (Inversion) as recommended by (Stocco, Godio & Sambuelli, 2009) which is the aim of reconstruct the model ( $m$ ) using a set of data measurements ( $d$ ) (Snieder & Trampert, 1999). Then, it can be assumed a mathematical derivation of a discrete problem as (Sacchi, 2006):

$$d = Gm \quad (4)$$

From equation 4 it can be concluded that the mathematical description of the physical process under study ( $G$ ) is crucial for both problems. As a result, in the next the mathematical description of the total magnetic field anomaly will be discussed. Only the case of induced magnetization is considered as the mineralogy of the study area is composed of paramagnetic and diamagnetic materials, which are characterized of having small and often negligible interactions between individual atomic magnetic moments (Lowrie, 2007).

### 2.4.1 Forward Modelling

The calculation of the direct problem enables us to compute the theoretical response due to magnetic source bodies, assuming some hypothesis on the shape, volume and the susceptibility contrast of the magnetic object, the hosting environment and the direction of the ambient magnetic field (Stocco, Godio & Sambuelli, 2009). To achieve this aim, several methods proposed by different authors (Talwani, 1965; Eirtzler et al., 1962; Kearey, Brooks & Hill, 2013; Won & Bevis, 1987; Liu et al., 2013) to construct the operator  $G$  were tested in order to check which worked for most of the variable polygonal shapes that could be proposed for the bodies underground.

One of the first methods tested was used by Talwani (1965) and Eirtzler et al. (1962) which follows the approach of Huberts (1948) of the line integral to compute gravitational attraction of 2-D objects having polygonal cross-section (Singh, 2002). A similar approach but assuming an

infinite length of the prism at one side was used by Kearey, Brooks & Hill (2013) and tested having a good response; however, it was necessary to take into account all the sides of the prism for complex body shapes. Another of the methods that were tested, as summarized by Singh (2002), was a more general formulation following the approach of Talwani (1959) for computing gravity and magnetic anomalies, which was presented by Won and Bevis (1987).

Even though the methods mentioned before had good responses, the method that was more efficient with different polygonal shapes of the magnetic body was the one used by Liu et al. (2013) which compute the magnetic anomaly using rectangular prism cells (**Figure 7**). In order to calculate the total field anomaly (TFA) is necessary to understand that it is the modulus difference between the total magnetic field and earth's magnetic field and is written as:

$$B = |\mathbf{B}| - |\mathbf{B}_0| \approx B_x \cos I_0 \cos A_0 + B_z \sin I_0 \quad (5)$$

Where  $\mathbf{B}$  is the total magnetic field vector,  $\mathbf{B}_0$  is the earth's magnetic field vector,  $B_x$  and  $B_z$  are the anomalous magnetic field components in the horizontal and vertical directions,  $I_0$  is the geomagnetic inclination and  $A_0$  is the angle between the profile and the geomagnetic north, and therefore  $A_0 = A - D_0$ , where  $A$  is the profile's geographical azimuth and  $D_0$  the geomagnetic declination (Liu et al., 2015).

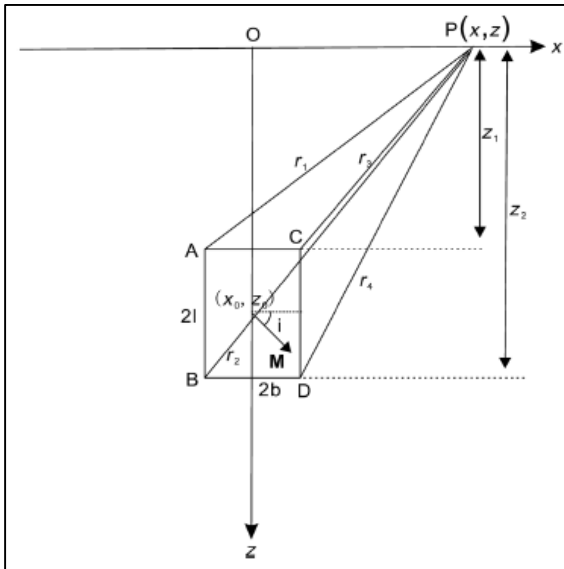


**Figure 7.** Rectangular prism (Taken from Liu et al., 2013).

Liu et al (2013) present the formulation of the magnetic fields that is given by (Liu et al., 2008):

$$\begin{aligned} B_x &= 2M \cdot [\sin I_0 \cdot \frac{E}{2} - \cos I_0 \cdot F] \\ B_z &= 2M \cdot [\cos I_0 \cdot \frac{E}{2} + \sin I_0 \cdot F] \end{aligned} \quad (6)$$

And following the rectangular prism (**Figure 7**):

$$\begin{aligned} E &= \ln \frac{(z_2^2 + x_2^2)(z_1^2 + x_3^2)}{(z_1^2 + x_1^2)(z_2^2 + x_4^2)} \\ F &= \tan^{-1} \frac{2bz_1}{z_1^2 + (x_1 - b)^2 - b^2} - \tan^{-1} \frac{2bz_2}{z_2^2 + (x_2 - b)^2 - b^2} \end{aligned}$$

Where  $x_1 = x_2 = x - x_0 + b$ ,  $x_3 = x_4 = x - x_0 - b$ ,  $z_1 = z_0 - z - l$ ,  $z_2 = z_0 - z + l$

In summary, this can be written in terms of equation 4 where the data values ( $d$ ) are going to be obtained by computing  $G$ , that is the total magnetic field vector  $B$  (equation 5), with  $m$  that is the model of magnetic susceptibilities ( $k$ ) together with the shape of the body, which are the main model parameters that are aimed to know their response.

### 2.4.2 Inversion

This is a mathematical technique that consists of gain the knowledge from the physical world by estimate some unknown attribute of interest in the support of inferences derived from observations, or measurements, that are indirectly related to this attributes by the means of mathematical techniques for reducing data (Vogel, 2002; Menke, 2012). The data analysis allows to make the derivation of model parameters that contain the essential description of the processes that are being studied which in this case is the total magnetic field anomaly. The model parameters and the data measurements can be represented as the elements of two vectors each one with length  $M$  and  $N$  respectively (Menke, 2012).

The principal affirmation of the inverse theory is that the data and model parameters are related with a quantitative model ( $G$ ) in the form of one or more formulas and in order to solve the inverse problem the simplest approach is an estimate of the model parameters ( $m^{est}$ ) by using  $G$  to translate the information from the data space into the model space (Tarantola, 2005; Menke, 2012). The measure of length of the estimated model parameters and the predicted data ( $d_i^{pre}$ ) with respect to the observed data ( $d_i^{obs}$ ) is relevant for the solution of the inverse problem as it dictates the error or misfit, which is  $e_i = d_i^{obs} - d_i^{pre}$  (Menke, 2012). There are different methods to measure this length, also known as the norm, but the most commonly used are:

$$L_1 \text{ norm: } \|e\|_1 = \left[ \sum_i [e_i]^1 \right] \quad (7. a)$$

$$L_2 \text{ norm: } \|e\|_2 = \left[ \sum_i [e_i]^2 \right]^{1/2} \quad (7. b)$$

$$L_n \text{ norm: } \|e\|_n = \left[ \sum_i [e_i]^n \right]^{1/n} \quad (7. c)$$

The best example of the use of this method is the least square solution (LSQ) which uses the  $L_2$  norm (Equation 7.b). In order to calculate the model parameters, the process is to compute the derivative of the error with respect to one of the model parameters and set the result to zero. After developing the process and presuming that  $[G^T G]^{-1}$  exist, the estimate of the model parameters is (Menke, 2012):

$$m^{est} = [G^T G]^{-1} G^T d \quad (8)$$

Even though this is a good attempt for an initial estimation of the model parameters, it is to simplify that is not the best approach. The reason is that equation 8 implicitly assumes that there is only one “best” solution to the inverse problem and this usually is not the case (Menke, 2012). This brings the need to know if the inverse problem can be classified as: 1) Undetermined problem, when there cannot be determined all the model parameters in a uniquely way with equation 4, or in other words where there are more unknowns than data ( $M > N$ ); 2) Even determined problem,

when  $M = N$  and there is zero prediction error and 3) Overdetermined problem, when  $N > M$  and the use of equation 8 is justified (Menke, 2012).

In practice, most of the inverse problems do not classify completely as undetermined or overdetermined, so they can be treated as “mixed-determined” problems and the sort of the unknown parameters into this two groups is the ideal approach to the solution of this type of problems (Menke, 2012). The singular-value decomposition (SVD) of the data kernel allow to accomplish this before mentioned partitioning of  $m$ ; however, as it is a time-consuming process, a different approach is used here (Menke, 2012). In this approach of the problem it is taken into account that the geophysical data is usually contaminated with errors and noise so equation 4 can be rewritten as (Sacchi, 2006):

$$Gm = d + e \quad (9)$$

Where  $e$  indicate the error or noise vector. This make that the optimization problem that needs to be solved is to minimize the combination of the Euclidean length of the model, also known as the model norm and the prediction error or misfit (Sacchi, 2006; Menke, 2012). This combination is the cost function  $J'$  that is given by (Sacchi, 2006):

$$\begin{aligned} J' &= \mu \text{Model Norm} + \text{Misfit} \\ &= \mu m^T m + e^T e \\ &= \mu m^T m + (Gm - d)^T (Gm - d) \end{aligned} \quad (10)$$

Minimizing as described before for the LSQ solution, subject to the  $L_2$  norm  $\|Gm - d\|_2^2 = \|e\|_2^2 = e^T e$ , the solution called damped least squares solution is (Sacchi, 2006):

$$m^{est} = (G^T G + \mu I)^{-1} G^T d \quad (11)$$

In this solution the trade-off parameter  $\mu$  play an important role as it can be deduced in equations 10. A large value of  $\mu$  give more importance to minimize the misfit in the model norm (Underfitting) while a small value of  $\mu$  indicate that in the minimization the model norm is the main term (Overfitting) (Sacchi, 2006). In order to choose the best value for  $\mu$ , the use of the “L-curve” is recommended.

Finally, if it is wanted to add smoothness to the estimated model, it is added a matrix of first or second order derivatives  $W$  in the cost function and after the minimization, the least squares weighted minimum norm solution is (Sacchi, 2006):

$$m^{est} = (G^T G + \mu W^T W)^{-1} G^T d \quad (12)$$

This last set of equations (10-12) are related with an abstract method known as Tikhonov regularization, which is meant to solve ill-posed problems, and iterative methods may be required in order to achieve this objective (Vogel, 2002). Some of the most known iterative methods are the steepest descent method, the conjugate gradient method and the Newton's method. The fundamental structure of all of them is basically the same as all starts at an initial point, according to a rule determine a direction of movement and then moves toward that direction which is ideally a minimum of the objective function (Luenberger & Ye, 1984). The rule by which it is determined the direction of movement is what makes them different from each other.

The method of steepest descent uses the negative gradient as the direction of the movement towards a minimum point from the initial one. For the Newton method, the rule is to devise a better solution  $m^{(p+1)}$  using the information about the shape of the error  $E(m)$  in the vicinity of  $m^p$ . This is done through a truncated Taylor series expansion of  $E(m)$  and then look for the minimum of that quadratic approximate function (Luenberger & Ye, 1984; Menke, 2012).

Conjugate gradient method is an intermediate between the steepest descent method and the Newton's method; it is one of the most used techniques as it is extremely effective with the optimization of general objective functions (Luenberger & Ye, 1984). It consist on obtain a new conjugate direction vector by evaluating the negative gradient vector at an iteration step  $k$  and adding a linear combination of the previous direction vectors (Luenberger & Ye, 1984).

### 3. Data Acquisition

The acquisition of the data through the magnetic method was developed by a field work in the study area from July 26 to 29 of 2018. As the topography was rough and there were some parts of the area with dense vegetation, four data lines were taken in the most suitable segments of the study area (Figure 8), with lengths of 140 m (Profile 1), 137 m (Profile 2), 179 m (Profile 3) and 144 m

(Profile 4). There were no electrical cables or near roads that could add noise and affect the acquisition of the data.

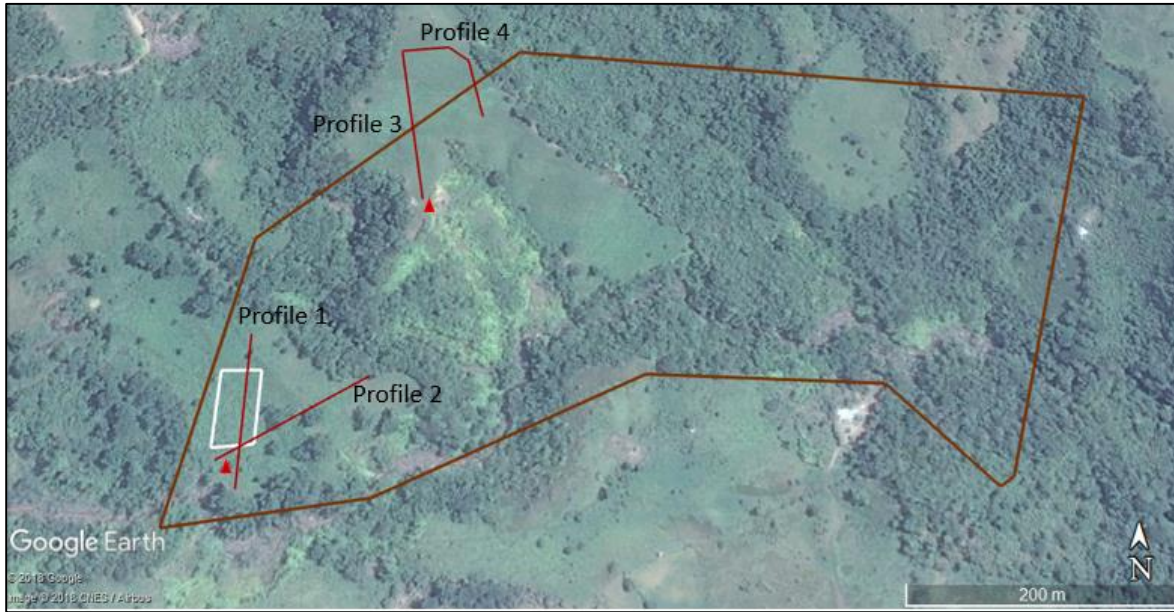


**Figure 8.** Aerial photography of the study area with the Profiles of magnetic data and the position of the base station as a red triangle. It is clear that the profiles were taken in the most suitable area within the mining title (taken from Google Earth).

The geophysical survey was carried out with two G-859 Caesium vapor magnetometers (an Optically Pumped magnetometer – see section 2.2.1) from Geometrics, with integrated WAAS/EGNOS enabled Tallysman GPS, one working as a base station and the other as a rover. The sensor sensitivity of the magnetometers is  $0.008 \text{ nT/Hz}$  RMS. The sampling interval of the profiles was of approximately 2 meters in order to avoid aliasing and the sensor height was approximately 2 m (the magnetic field varies less with elevation than the gravity field, so it is not necessary to collect accurate height information during a survey (Dentith & Mudge, 2014)).

The line directions were selected with the aim to cover all the possible parts of the study area and also to be perpendicular to the geologic structures inferred during the field work and documented in the geological map (**Figure 4**). Following the above mentioned, two of the profiles (Profiles 1 and 3) were taken in an S-N trend and the other profiles (Profiles 2 and 4) perpendicular or crossing the first two ones.

## 4. Results

### 4.1 Benchmark of the code

In order to corroborate the anomaly given by the code, it was compared with anomalies calculated with analytical formulas. The first one was the dipole/ finite dike (**Figure 9**), which anomalies for different inclinations are presented by Telford, Geldart, & Sheriff (1990), Eirtzler et al. (1962) and also explained by Lowrie (2007).

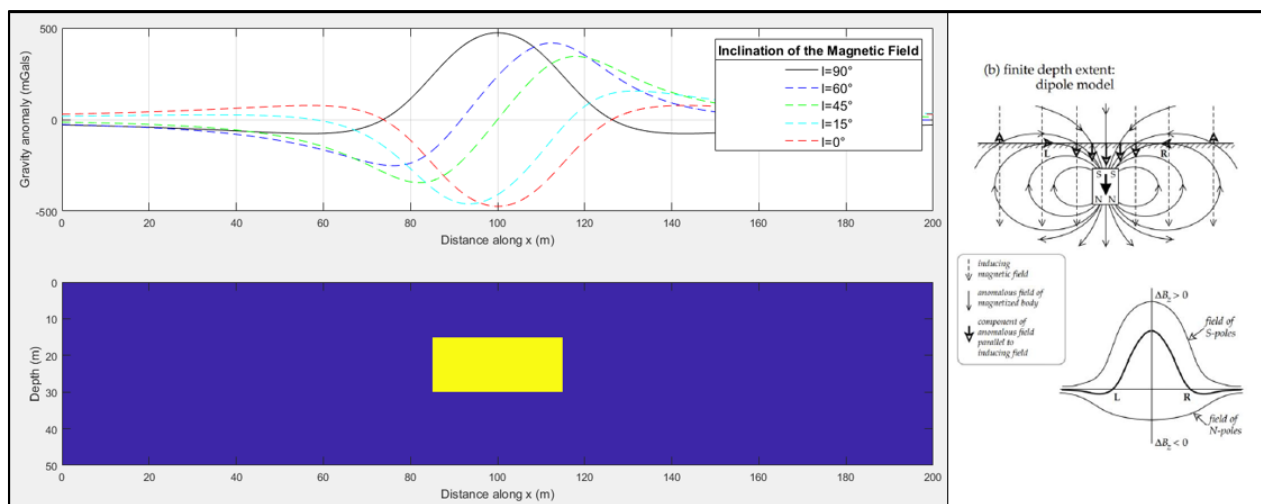


**Figure 9.** Anomaly of a finite dipole with different inclinations. The one with the continuous line represent the anomaly with an inclination of  $90^\circ$  and at the right is the explanation given by Lowrie (2007) (modified from Lowrie, 2007). The model have a susceptibility of  $k = 3 \times 10^{-3} (SI)$ ,  $M = 31000 \text{ nT}$  and  $A_0 = 0^\circ$ . The inclination tested values were  $I_0 = 90^\circ, 60^\circ, 45^\circ, 15^\circ$  and  $0^\circ$ .

Another example from Lowrie (2007) tested by the code was the effect of block width with the anomaly shape following the three cases considered by the author (the block was placed with the top at a depth of  $9 \text{ m}$  and the base at a depth of  $12 \text{ m}$ ). The three cases are: a narrow block of width  $w = (2m) = 18 \text{ m}$  for which  $m/z_1 = 1$ , a block of width  $36 \text{ m}$  ( $m/z_1 = 2$ ) and a wide block of width  $144 \text{ m}$  ( $m/z_1 = 8$ ) (In a model with an extent of  $400 \text{ m}$  and a depth of  $80 \text{ m}$ ).

As can be seen in **Figure 10**, even though the values are not the same as the example presented by Lowrie (2007), the shapes of the anomalies are almost the same because the ratio between the width and the depth were equal in both models. Also, it is important to take into account that the anomalies presented by Lowrie (2007) were calculated using the “planar angles subtended at the point of measurement by the top and bottom edges of the vertically magnetized crustal block” (Lowrie, 2007) (see **Figure 10**) which is a different way of the tested code.

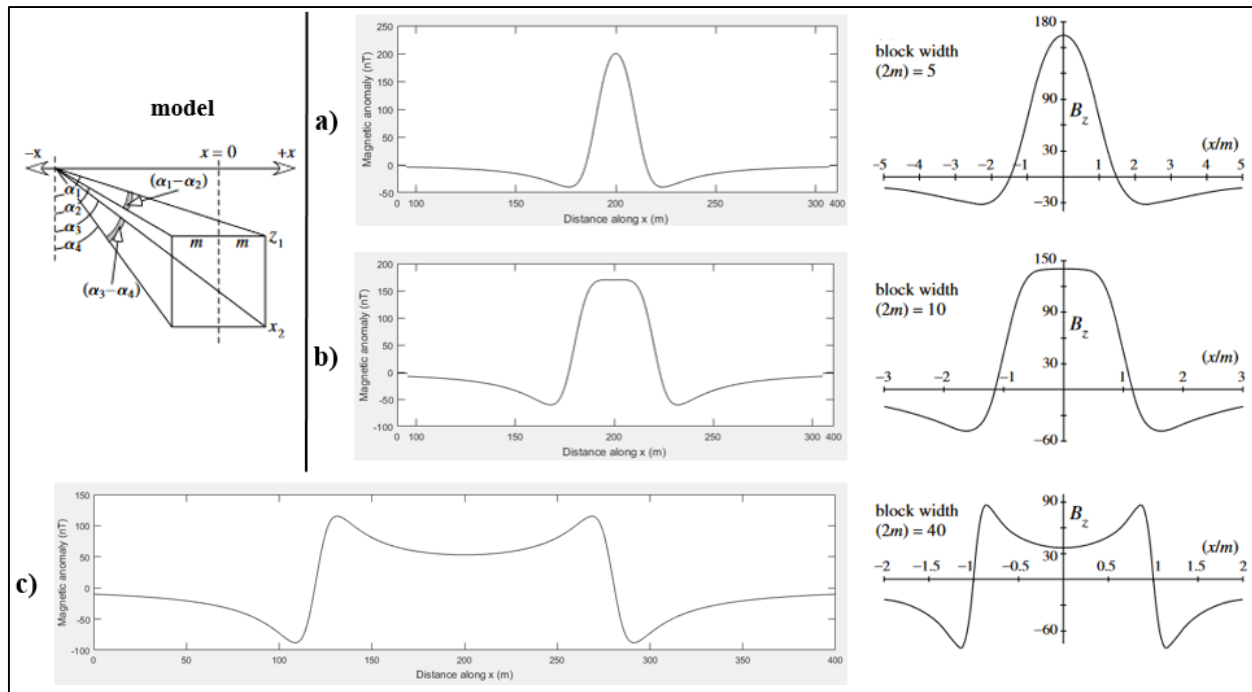


**Figure 10.** Comparison of the shape of the anomaly of a vertically magnetized ( $I_0 = 90^\circ$ ) crustal block in which **a)**  $m/z_1 = 1$ , **b)**  $m/z_1 = 2$  and **c)**  $m/z_1 = 8$ . It can be seen that the block widens with respect to its depth, its amplitude decreases and the negative lobes grow. At the left side is the model followed by Lowrie (2007) to calculate the anomaly (modified from Lowrie, 2007).

Finally, it was necessary to test the shape of the anomaly generated by a dipping sheet as it is going to be useful for the expected model of the mineralization of the study area. For this aim it was used the parameters of an example presented by Telford, Geldart & Sheriff, (1990) and also it was compared with the anomaly shapes of a slanted body presented by Eirtzler et al. (1962) (**Figure 11**).

It is clear that the shape of the anomaly differs between **Figure 11.a** and **Figure 11.b** because, even though it was stated the same value for the geomagnetic inclination, they have different

directions. In order to be able to compare the response of the code with the example of the mentioned authors, it was necessary to change the direction of the geomagnetic inclination as is shown in **Figure 11.c** by modifying the sign in the code. The shape of the anomaly generated by the dipping sheet (**Figure 11.c**) now correlates with the example presented by Telford, Geldart & Sheriff, (1990) as the shallower part of the body is associated with the negative anomaly (as it can be seen too in **Figure 11.b**) and the deepest part is associated with the positive anomaly.

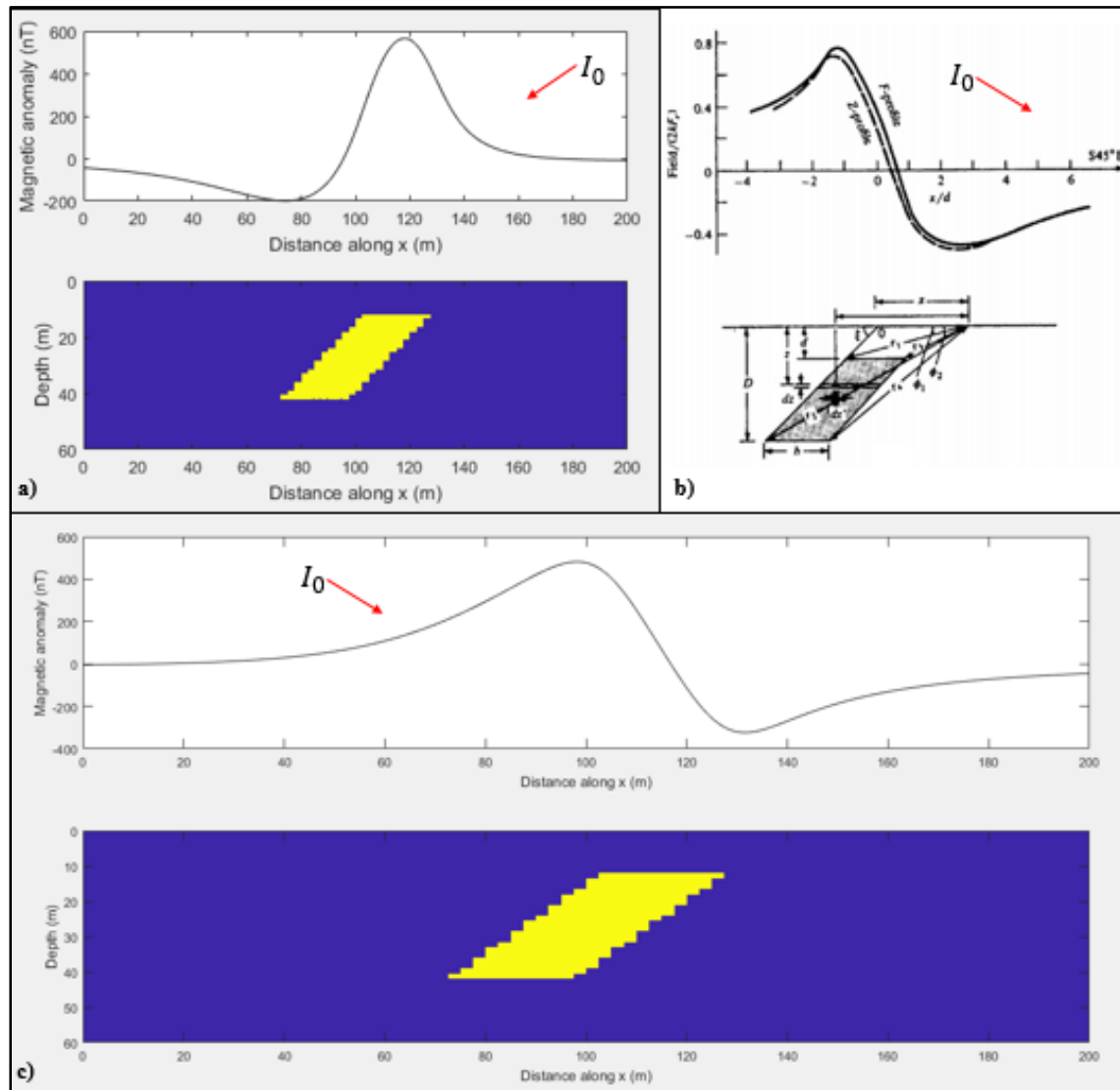


**Figure 11.** Profiles for a dipping sheet for  $I_0 = 60^\circ$ ,  $A_0 = 45^\circ$ ,  $Dip = 45^\circ$ ,  $b = 2d$ ,  $D = 3.5d$  (with  $d = 12$  m,  $M = 30000$  nT and  $k = 3 \times 10^{-3}$  (SI) in the model) (modified from Telford et al., 1990) where **a**) is the response of the code, **b**) is the example presented by Telford et al. (1990) and **c**) is the response of the modified code.

## 4.2 Synthetic example

For the synthetic example, a model for the mineralization with the shape of a dipping sheet was proposed. The reason for this is based on **Figure 5** and several cross-sections of other mines of the zone in which associate the emerald deposits to the hydrothermal breccia. As a summary of the description developed in the geological frame (see section 1.1), the emerald deposits are usually present in calcite veins or breccia with associated pyrite that can have 3 m width and this structures are most commonly found in black shales. In this way, the model of magnetic susceptibilities (Table 1) will follow this general description of the zone.

Mineral/Rock	Susceptibility $\times 10^3$ (SI)	
	Range	Average
Shales	0.01-15	0.6
Calcite	-0.001 - -0.01	-
Pyrite	0.05-5	1.5

**Table 1.** Magnetic susceptibilities of the model (Taken from Telford, Geldart & Sheriff, 1990).

In addition to the characteristics before mentioned, it is crucial to define the induced magnetic field parameters of the study area (Table 2) as it was seen in the previous section that they have a significant influence in the estimation of the magnetic anomaly of the proposed model (also see equations 5-6). Having already mentioned all the important parameters, it is proposed a breccia of approximately 2.5 m width (supposing that it predominates the calcite characteristics, with a magnetic susceptibility of  $k = -0.008 \times 10^{-3}$ (SI)) that is in a black shale with a magnetic susceptibility  $k = 0.6 \times 10^{-3}$ (SI) (**Figure 12.a**).

Modeling Parameters (from the IGRF)		
$I_0$ - Inclination (°)	$D_0$ - Declination (°)	$M$ - Total field intensity (nT)
29.2142	-7.4913	31076.2

**Table 2.** Induced magnetic field parameter values over the study area in the date of the data acquisition (Taken from the International Geomagnetic Reference Field (IGRF-12)).

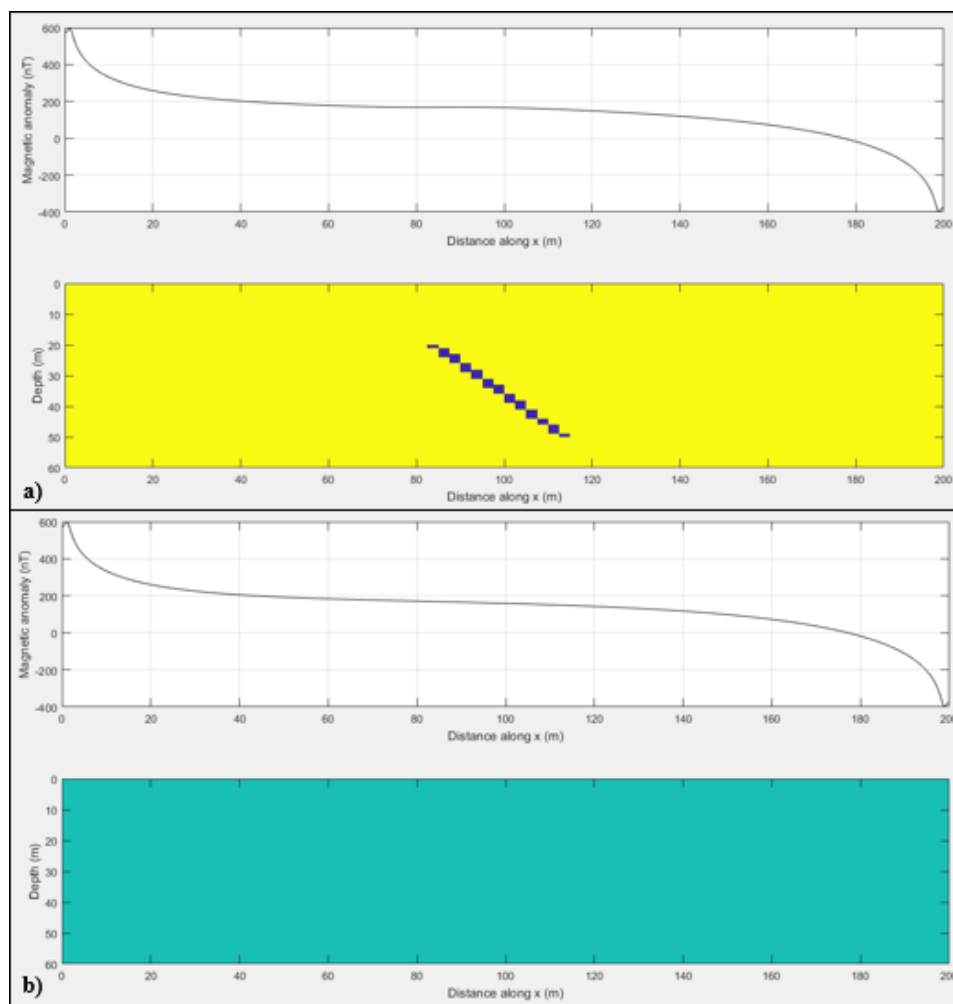


**Figure 12.** *a)* Breccia of calcite of approximately 2.5 m. It is modeled as a dipping sheet because of the structural geology of the zone. Dip angle of  $45^\circ$  and the magnetic field parameters are the ones mentioned in **Table 2.** *b)* A model with only the magnetic susceptibility of the black shale which is the background of (a).

As the extension of the model is too large and the dipping sheet has a wide expansion, the anomaly generated by the structure is also wide and is lost in the regional anomaly. This can be solved if the regional anomaly (the response of a model with the properties of the background - **Figure 12.b**) is removed. The effect of this can be seen in **figure 12.c**, where the anomaly of the dipping sheet is clear. Another observation that can be derived from comparing this with **figure 12.d** is that it is important to take into account the contrast in the magnetic susceptibilities of the body with the medium as the magnitude of the anomaly differs from a model in which the breccia (with the same value of magnetic susceptibility) is embedded in a nonmagnetic medium.

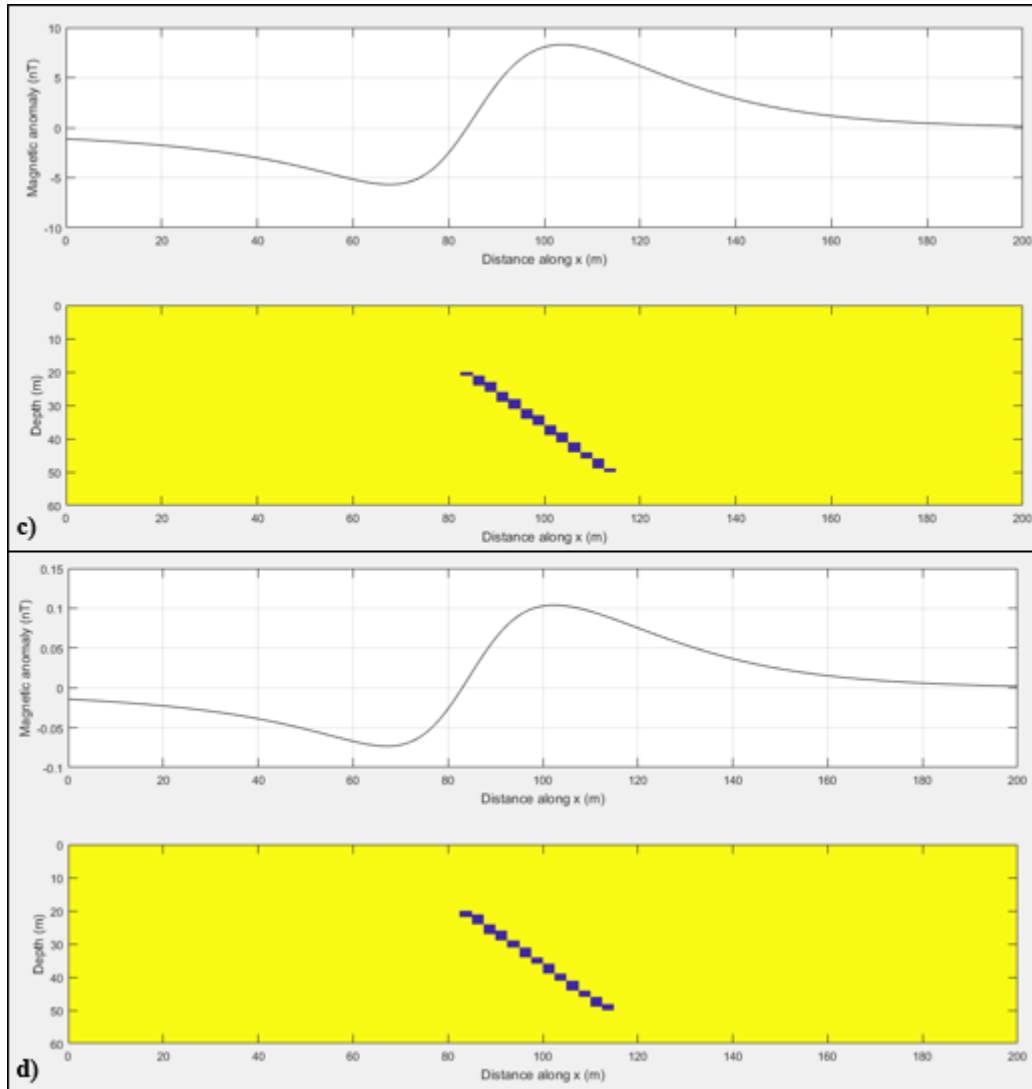


**Figure 12. (Continued)** *c) Anomaly of the same breccia of calcite (a) but without the effect of the background (b). d) The anomaly of the breccia calcite embedded in a nonmagnetic medium. Notice that the difference in the magnitude of the anomaly differs in almost two orders of magnitude.*

**Figure 13** shows the forward model of the cross section of a mine next to the study area (Tequendama mine - **Figure 5**) in which the associated pyrite in the breccia and the different types of black shale were added. The same process developed in **Figure 12** is applied to obtain this response (see **Appendix A**) which means that even though in the **Figure 13** the magnetic properties of each proposed structure is defined separately, the anomaly was calculated using the contrast between them.

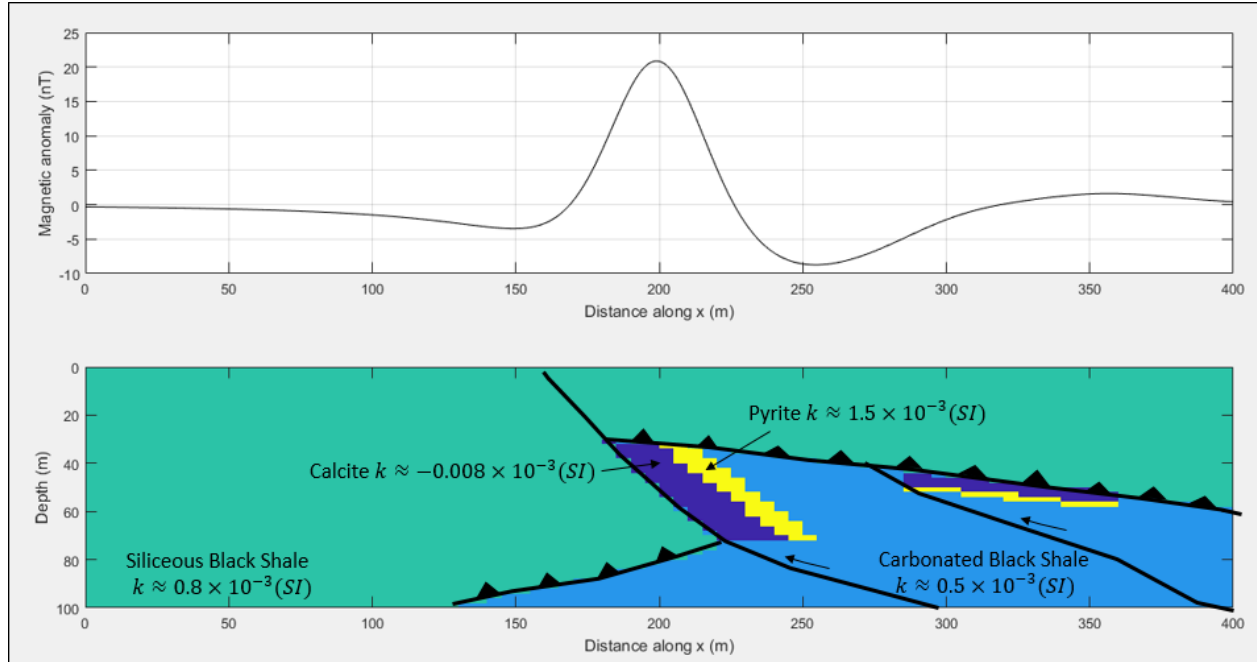


**Figure 13.** Model of the mineralization of the zone. The top of the biggest breccia is at 30 m and is dipping with an angle of  $45^\circ$ . The magnetic field parameters are the ones mentioned in **Table 2**.

### 4.3 Synthetic data inversion

In order to test the algorithms presented in section 2.3.2, a synthetic data derived from the forward model of a dipping sheet was used (**Figure 14**). The algorithms used were the simple least squares, the damped least squares, the weighted damped least squares and the conjugate gradient (which uses a simple least squares algorithm but is an iterative method).

The results of the application of the algorithms confirms that the simple least squares method (**Figure B1, B4**) is inefficient as this is a problem with an undetermined component and, as a result, the amount of data is insufficient to constraint the estimation of the model parameters. In other words, “least squares fails [because] the number of solutions that give the same minimum prediction error is greater than one” (Menke, 2012). This evident importance of the inclusion of constraints in the inversion problems is taken into account by the damped least squares as it include a restriction related with the model norm (see section 2.3.2), which is a way to add *a priori* information to the inverse problem (the selection of the trade-off parameter was done with the use

of the L-curve method – **Figure C1**). In the case of the weighted damped least squares method it is also included a constraint in the variations of the parameters of the model by the use of a matrix of first order derivatives.

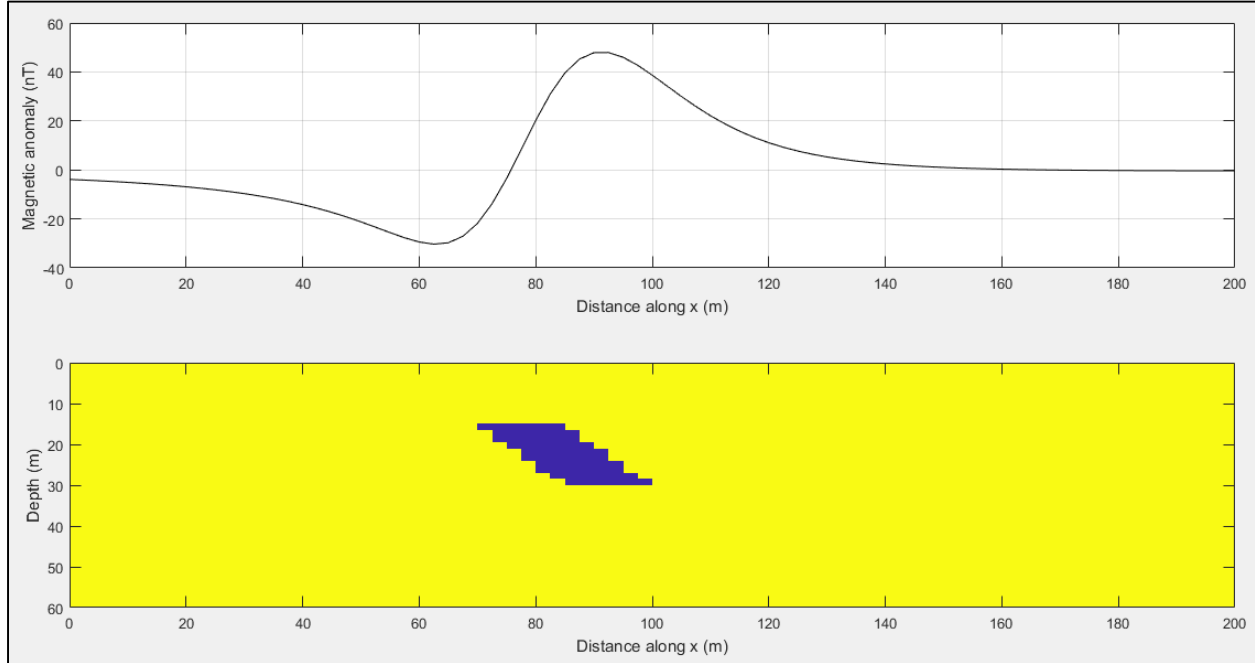


**Figure 14.** Synthetic data and the model of magnetic susceptibilities (where the dipping sheet has a magnetic susceptibility of  $k = -0.008 \times 10^{-3}$  (SI) and the background a  $k = 0.6 \times 10^{-3}$  (SI)). The model is divided in 40 by 80 prisms and the magnetic field parameters are the ones mentioned in **Table 2**.

As it can be seen in **Figure B2, B3**, this included *a priori* information improved the inversion algorithm as a negative value of magnetic susceptibility was placed near the surface, just above the real model. The problem of the inversion in this case (which was to concentrate the structures near the surface), is not related to the parameter estimation but with the natural decay of the amplitude of the magnetic anomaly with depth (Li & Oldenburg, 1996). This issue is typical of potential methods as explained by Li & Oldenburg (1996) and they propose to add a depth weighting so this can be overcome.

#### 4.4 Real data inversion

For the inversion of the real data the damped least squares method was used as it was one of the best approaches in the synthetic data inversion. It is resolved to apply this algorithm to the Profile 1 as it was developed over a possible fault zone that was inferred during the field work and seems

to be associated with the Itoco fault (**Figure 16**). As the depth weighting proposed by Li & Oldenburg (1996) was not included in the algorithm, the structures that the anomaly generated are concentrated near the surface as it was expected.

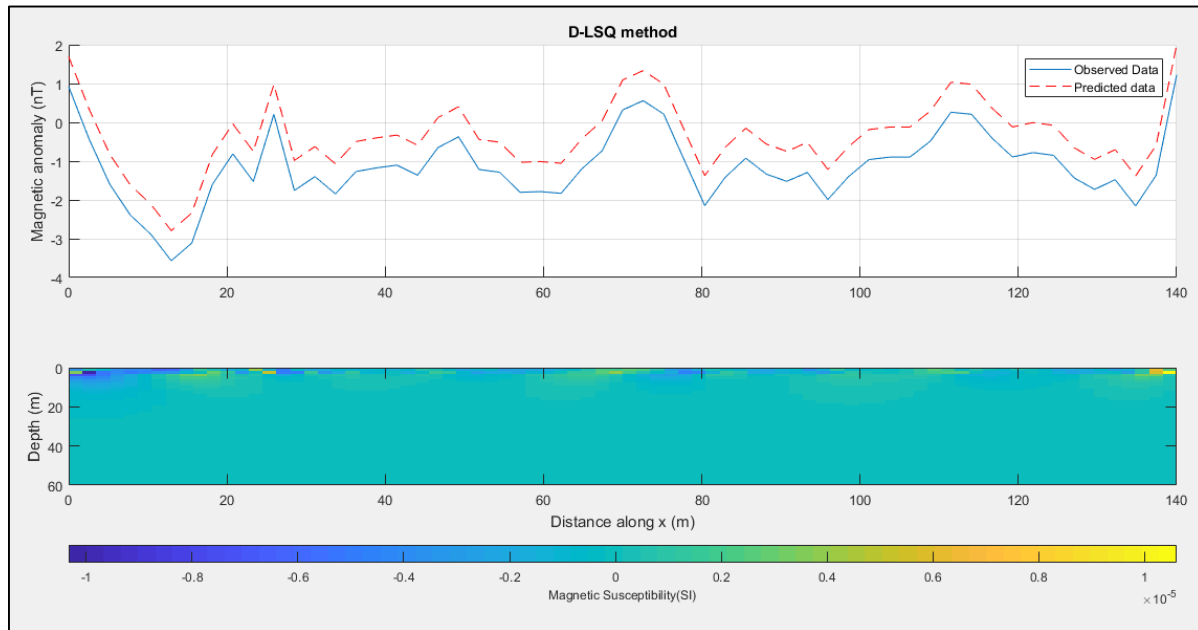


**Figure 15.** 2D magnetic susceptibility model generated with damped least squares inversion method for the profile 1 (with a rms error of 0.6 nT).  $I_0 = 29.2142^\circ$  and  $D_0 = -7.4913^\circ$ .

#### 4.4.1 ZondGM2D Results

The use of constraints in the inversion method as well as in the mathematical description is crucial for a good estimation of the model parameters, as can be concluded from the previous sections. In this way, a software for 2D interpretation of magnetic and gravity data called ZondGM2D was used in order to have a more advanced inversion. To follow the same structure of the magnetic data modelling process, the forward model of the software is tested first, in which the mathematical description of the model (G) is calculated with the same equation 5.

The inversion is developed with the Occam method, which is comparable with the weighted damped least squares method. This relation is explained as the Occam algorithm include a trade-off parameter (also known as regularizing parameter); however, as the cost function is described with nonlinear data functionals the procedure is to set a value of tolerance, linearize the cost

function and solve it iteratively (de Groot-Hedlin & Constable, 1990). A matrix of partial derivatives of measured data with respect to model parameters ( $A$ - Jacobian) and a vector of residuals between the observed and calculated values ( $\Delta f$ ) are introduced in order to minimize the perturbations about a starting model.

Moreover, it includes other constraints by adding a matrix of relative measurement errors ( $W$ ) so that “the smoothest model is sought subject to the criterion that it fit the data to a statistically reasonable tolerance” (de Groot-Hedlin & Constable, 1990). A smoothing operator ( $C$ ), which is a measure of the model roughness, is included to prevent high variability in the parameters in horizontal and vertical directions. Finally, the equation for the inversion in matrix notation (Kaminsky, 2001):

$$(A^T W^T W A + \mu C^T C) \Delta m = A^T W^T \Delta f - \mu C^T C m \quad (13)$$

To benchmark this method implemented in the software, the inversion of the synthetic data used in the section 4.3 was developed. As it can be seen in **Figure 16**, even though the shape of the dipping body is not well described, the position in the 2D model of magnetic susceptibilities obtained by the inversion method is correct.

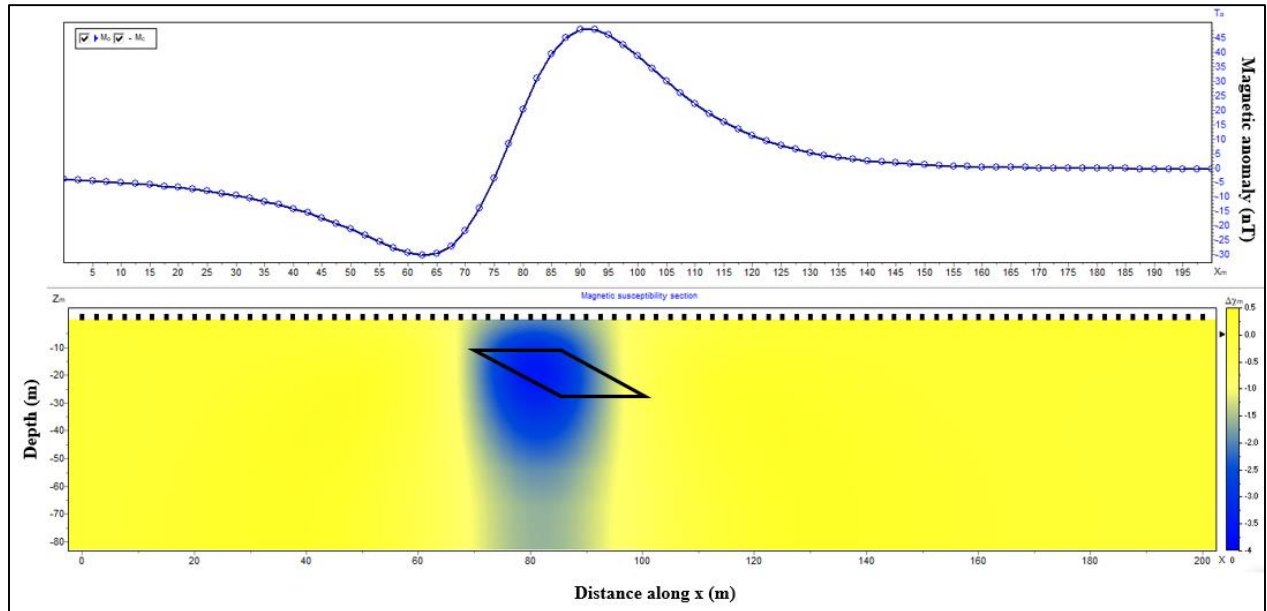


**Figure 16.** Results of the inversion of the synthetic data with the Occam method using the software ZondGM2D with parameter values of  $I_0 = 29.2142^\circ$  and  $D_0 = -7.4913^\circ$ . The magnetic susceptibility contrasts are in  $10^{-5}$  CGS units. The contour demark the shape of the proposed body. (Rms error of 0.0012).

In terms of the value of the magnetic susceptibility contrasts, the value assigned in the synthetic model was of  $k = -0.608 \times 10^{-3}$ (SI) (magnetic susceptibility contrast between the black shale and the calcite) and the value obtained was of  $k = -0.465 \times 10^{-3}$ (SI) (To convert values in SI system, magnetic susceptibility in CGS system, which in this case is  $k = -0.037 \times 10^{-3}$ (CGS), is multiplied by  $4\pi$ ). This is a good approximation as it is in the same order of magnitude.

Having already checked the correct operation of the program, the inversion of the profile 1 (**Figure 17**) and profile 2 (**Figure 18**) were performed since, as stated before, these were taken in an area where there is possibly a fault and mineralization is more likely. The values of the code are a regularization parameter of 1, smooth factor of 0.05 and 10 iterations; induced magnetic field parameter values of the study area are  $I_0 = 29.2142^\circ$  and  $D_0 = -7.4913^\circ$  (**Table 2**) and the magnetic susceptibility contrast ( $\Delta\chi_m$ ) is expressed in  $10^{-5}$  CGS system.

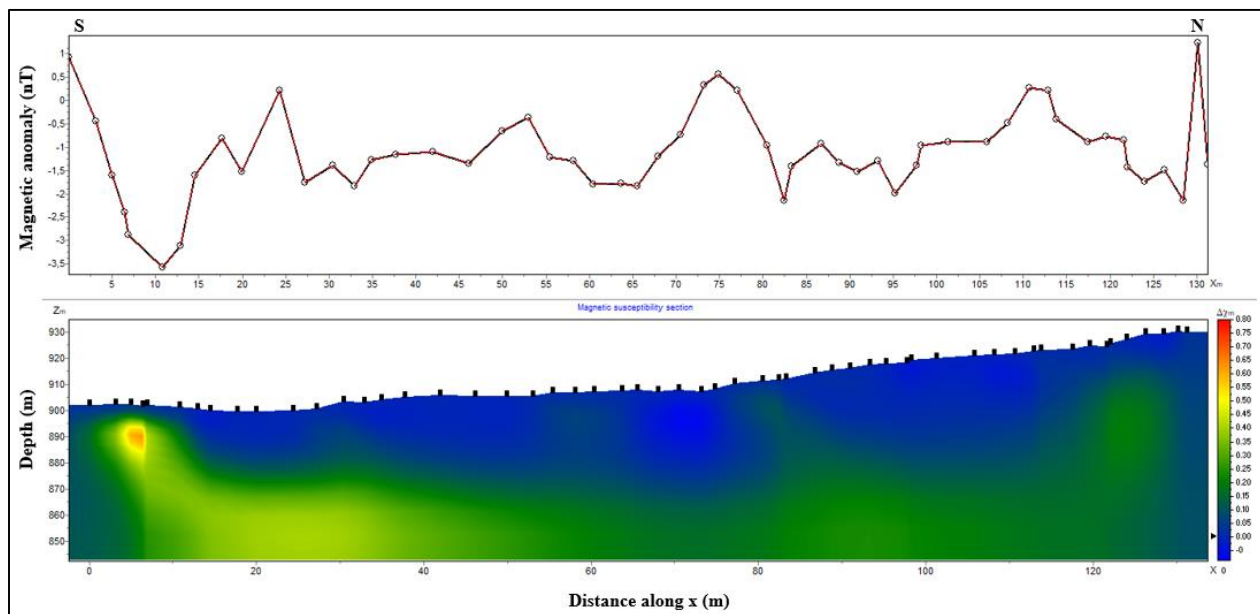


**Figure 17.** 2D Model of Magnetic susceptibilities for Profile 1 (azimuth  $A = -3.8^\circ$ ). Rms error of 0.065. Dashed red line represent the estimated values. The values of  $\Delta\chi_m$  vary between  $-0.02 \times 10^{-5}$  (CGS) and  $0.8 \times 10^{-5}$  (CGS).

Something important to point out is that the intervals of the magnetic susceptibilities in the model, converted to  $10^{-3}$  SI system, are in the range of the expected magnetic susceptibilities presented in **Table 1**. In addition, as it can be seen in **Figure 17** and **Figure 18**, another interesting characteristic of the software is that it includes the topography of the study area. This allowed me

to verify that the effects of the topography for this survey are irrelevant (as stated in section 2.3) because the inversion of the profiles without this characteristic do not present significant changes (see **Appendix D**).

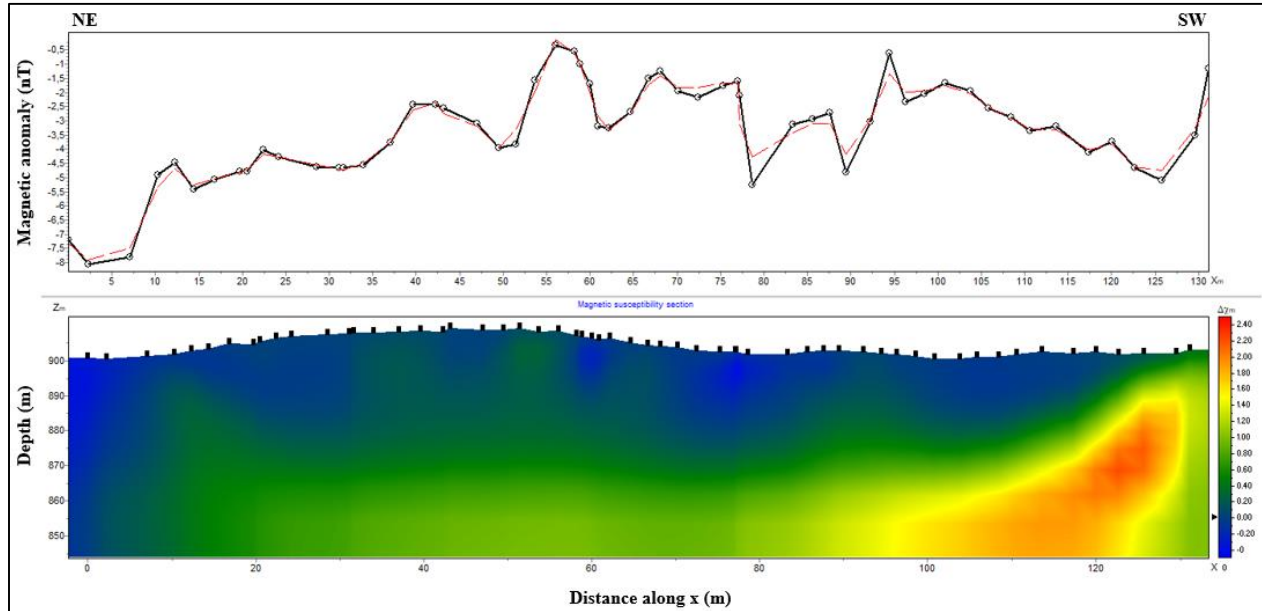


**Figure 18.** 2D Model of Magnetic susceptibilities for Profile 2 (azimuth  $A = -122^\circ$ ). Rms error of 0.51. Dashed red line represent the estimated values. The values of  $\Delta\chi_m$  vary between  $-0.5 \times 10^{-5}$  (CGS) and  $2.5 \times 10^{-5}$  (CGS).

## 5. Discussion

The magnetic data modelling was developed following two important main steps. The results of the Forward modelling (First step) allow to test and improve G by computing it with several 2D magnetic susceptibility models and comparing the responses with the literature (Telford, Geldart, & Sheriff, 1990; Lowrie, 2007). Several techniques for a 2D model (Talwani, 1965; Eirtzler et al., 1962; Won and Bevis, 1987) were tested but the one developed by Liu et al. (2013) which compute the magnetic anomaly using rectangular prism cells was selected. It was interesting to see the influence of the variation of parameters such as the magnetic field parameters, magnetic susceptibility, shape, size and depth of the structures in the medium.

Even though the responses were correct in the case of simple shapes (finite dike or crustal block) for all the techniques implemented, when more complex models were proposed the solutions did not expressed the expected results. This may be due to the fact that special care must be taken when

introducing angles in the calculation of magnetic anomalies or, in the case of Kearey, Brooks & Hill (2013) that all boundaries need to be taken into account.

At the time of generating the synthetic models a problem was seen when a magnetic susceptibility value was added to the medium. This was because the code took this as a block and calculated the corresponding anomaly. The way to solve this was by subtracting the properties of the medium, which is the same as taking into account only the contrasts of the magnetic susceptibilities of the bodies within it. The outcome of this was that the contrast of the magnetic properties in the medium is what prevails and must be taken into account in terms of the calculation of magnetic anomalies.

Regarding to the inversion process (second step), it was evident that when this was not constrained, the least squares method failure was inevitable. This is because, as declared before, the problem has a large undetermined component so the need for more information that counteract this issue is essential. To mention one of the multiple possible options, a correction related with the natural decay of the magnetic field with distance to the point of measure can be implemented. This is performed by adding a depth weighting matrix to the inversion algorithm, a method implemented with the aim to avoid the concentration of the magnetic susceptibility contrasts in the surface (Li & Oldenburg, 1996).

The statement of the relationship between adding more constraints and a more reliable model is proven with the use of the software ZondGM2D. The inversion of the synthetic data with the program demonstrated the accuracy of this when determining the position of the contrast of magnetic susceptibilities and also on the estimation of the magnetic susceptibility contrasts. However, it can be seen how the software had some complications in estimating the real shape of the object under study (**Figure 16**). For this reason, it is recommended to implement the method proposed by Lelièvre (2009) which consists of modifying the values of the smoothing weights, by using one of the methods proposed by the author, to generate a smoothing of the model in another direction (as an example, the most probable trend of the structures in a zone).

## 5.1 Geological interpretation of the models

The 2D models of magnetic susceptibilities obtained by the inversion of the profiles mentioned in the last section were compared with the geological map and background in order to propose a

coherent and credible geological interpretation (**Figure 19**). In the first place, a structural analysis was developed as, according to **Figure 4** and **Figure 8**, the profiles 1 and 2 were developed over the Itoco fault. For the profile 1 (**Figure 19.a**), it can be seen that according to the contrast of magnetic susceptibility two dipping trends were interpreted, one since the beginning of it and the other one at around 80 m.

In the case of the profile 2 (which is more perpendicular to the structure) in the model it also can be interpreted a dipping trend towards the northeast, in this case at the end of the profile (which is the most southern part) and the other one around 90 m from the beginning of the profile. Joining this to what was observed in the field, one of the trends was interpreted as the Itoco fault or a related fault derived from this one (**Figure 19**) and the other one can be some fault associated. However, there is no information about the presence of this one neither in the geological map nor in the observations of the field which gives way to infer that it might be related with the mineralization.

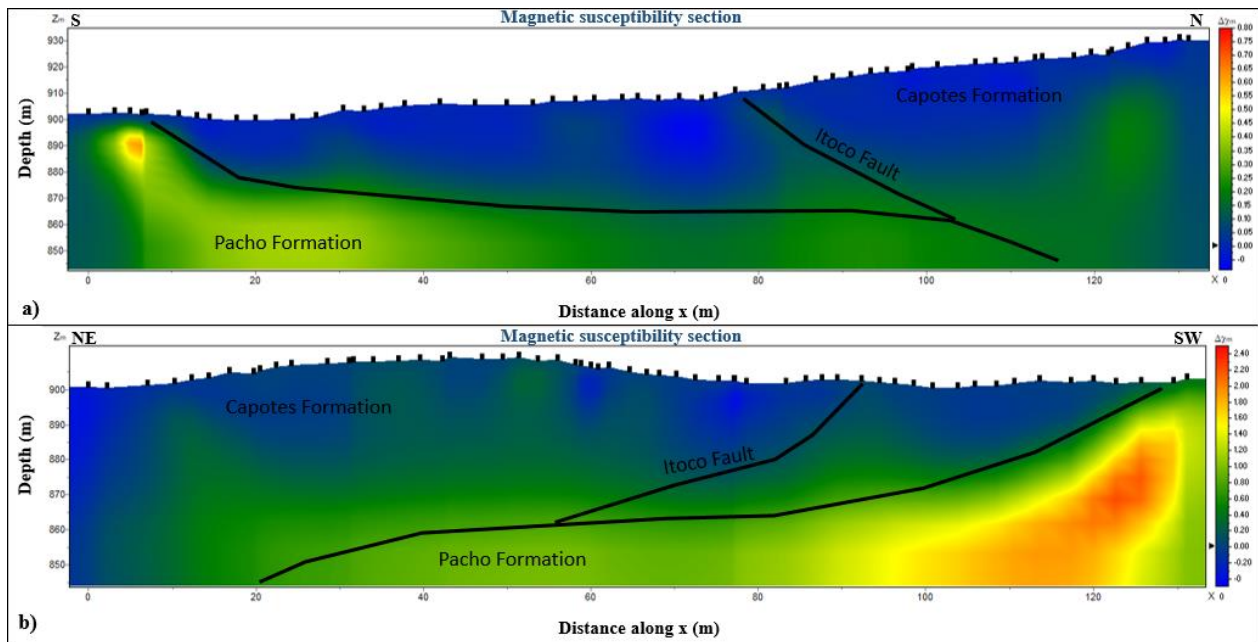


**Figure 19.** Geological interpretation of the 2D models of magnetic susceptibilities for a) Profile 1 and b) Profile 2.

After this structural analysis of the model, the contrasts of magnetic susceptibilities are analyzed. In general terms, the model can be divided into two large main groups with similar characteristics; one of almost zero to negative values and another one with positive small to high values of contrasts of magnetic susceptibilities. In this way, it can be interpreted that the Capotes

formation (which is mostly composed by carbonated shales) (Reyes et al., 2006) is related with the lower magnetic susceptibilities and the Pacho formation (siltstone, claystone and quartz sandstones, shales) (Reyes et al., 2006) is related with the higher magnetic susceptibilities. The presence of positive contrast of magnetic susceptibilities in the interpreted carbonated black shales might be the result of a possible mineralization.

## **6. Conclusions**

The magnetic susceptibility models obtained by the forward model and the inversion of the data acquired in the study area allowed to expand the knowledge of this zone of emerald potential. Each of the methods applied gave a different approach to the problem but together contributed to a complete understanding of the geophysical survey. The forward model gave the relevant predictions of the response of the magnetic method application (in terms of anomaly shape and magnitude) with the magnetic field parameters of the area and the assumption of the presence of the mineralization and its most plausible shape according to the geology.

The inversion algorithm implemented in the ZondGM2D software gives the necessary constraints to the least squares inversion method in order to take advantage of the model parameters that can be inferred from the acquired data. The reliability and accuracy of the response of the software implementation was proven first with the inversion of synthetic data. Then, two 2D models of magnetic susceptibility were calculated for the study area and an interesting result was obtained as the models showed the possible structure of the Itoco fault, which is one of the structures related with the emerald deposits of the zone.

## References

- Bayona, G., Cortés, M., Jaramillo, C., Ojeda, G., Aristizabal, J. J., & Reyes-Harker, A. (2008). An integrated analysis of an orogen–sedimentary basin pair: Latest Cretaceous–Cenozoic evolution of the linked Eastern Cordillera orogen and the Llanos foreland basin of Colombia. *Geological Society of America Bulletin*, 120(9-10), 1171-1197.
- Branquet, Y., Cheilletz, A., Giuliani, G., Laumonier, B., & Blanco, O. (1999). Fluidized hydrothermal breccia in dilatant faults during thrusting: the Colombian emerald deposits. *Geological Society, London, Special Publications*, 155(1), 183-195.
- Cook, F. A. (1997). Applications of geophysics in gemstone exploration. *Gems & Gemology*, 33(1), 4-23.
- Cooper, M. A., Addison, F. T., Alvarez, R., Coral, M., Graham, R., Hayward, A. B. & Pulham, A. J. (1995). Basin development and tectonic history of the Llanos Basin, Eastern Cordillera, and middle Magdalena Valley, Colombia. *AAPG bulletin*, 79(10), 1421-1442.
- deGroot-Hedlin, C., & Constable, S. (1990). Occam's inversion to generate smooth, two-dimensional models from magnetotelluric data. *Geophysics*, 55(12), 1613-1624.
- Dentith, M., & Mudge, S. T. (2014). *Geophysics for the mineral exploration geoscientist*. Cambridge University Press.
- Eirtzler, J. R., Peter, G., Talwani, M., & Zurflueh, E. G. (1962). *Magnetic anomalies caused by two-dimensional structure: their computation by digital computers and their interpretation* (No. TR-6). Lamont Geological Observatory Palisades NY.
- Giuliani, G., Dubessy, J., Ohnenstetter, D., Banks, D., Branquet, Y., Feneyrol, J. & Martelat, J. E. (2017). The role of evaporites in the formation of gems during metamorphism of carbonate platforms: a review. *Mineralium Deposita*, 53(1), 1-20.
- Groat, L. A., Giuliani, G., Marshall, D. D., & Turner, D. (2008). Emerald deposits and occurrences: A review. *Ore Geology Reviews*, 34(1-2), 87-112.

Jimenez Guevara, J. F. (2017) *Estudio químico, mineralógico y espectroscópico de esmeraldas colombianas de los distritos mineros de Chivor, Muzo y Coscuez y su aplicación en la determinación de origen geográfico* (Doctoral dissertation, Universidad Nacional de Colombia-Sede Bogotá).

Kaminsky, A. (2001). ZondGM2D [Computer Software]. Saint-Petersburg. Retrieved from <http://zond-geo.com/english/zond-software/>

Kearey, P., Brooks, M., & Hill, I. (2013). *An introduction to geophysical exploration*. John Wiley & Sons.

Lelièvre, P. G. (2003). *Forward modelling and inversion of geophysical magnetic data* (Doctoral dissertation, University of British Columbia).

Li, Y., & Oldenburg, D. W. (1996). 3-D inversion of magnetic data. *Geophysics*, 61(2), 394-408.

Liu, S., Hu, X., Liu, T., Feng, J., Gao, W., & Qiu, L. (2013). Magnetization vector imaging for borehole magnetic data based on magnitude magnetic anomaly. *Geophysics*, 78(6), D429-D444.

Liu, S., Hu, X., Xi, Y., Liu, T., & Xu, S. (2015). 2D sequential inversion of total magnitude and total magnetic anomaly data affected by remanent magnetization. *Geophysics*, 80(3), K1-K12.

Lowrie, W. (2007). Geomagnetism and paleomagnetism. In *Fundamentals of Geophysics* (pp. 281-362). Cambridge: Cambridge University Press. doi:10.1017/CBO9780511807107.006

Luenberger, D. G., & Ye, Y. (1984). *Linear and nonlinear programming* (Vol. 2). Reading, MA: Addison-wesley.

Maya, M., Buenaventura, J., & Salinas, R. (2004). Estado del conocimiento de la explotación de esmeraldas en Colombia. *Ministerio de Minas y Energía. Instituto Colombiano de Geología y Minería*.

Menke, W. (2012). *Geophysical data analysis: Discrete inverse theory*. Academic press.

Parra, M., Mora, A., Jaramillo, C., Strecker, M. R., Sobel, E. R., Quiroz, L., ... & Torres, V. (2009). Orogenic wedge advance in the northern Andes: Evidence from the Oligocene-Miocene sedimentary record of the Medina Basin, Eastern Cordillera, Colombia. *Geological Society of America Bulletin*, 121(5-6), 780-800.

Pignatelli, I., Giuliani, G., Ohnenstetter, D., Agrosi, G., Mathieu, S., Morlot, C., & Branquet, Y. (2015). Colombian Trapiche Emeralds: Recent Advances in understanding their Formation. *Gems & Gemology*, 51(3).

Reyes, G., Montoya, D., Terraza, R., Fuquen, J., & Mayorga, M. (2006). Memoria geología del cinturón esmeraldífero occidental.

Sacchi, M. D. (2006) *Intro to Inverse Problems in Exploration Seismology*. Seismic Imaging Summer School. University of Calgary, Calgary, Canada.

Singh, B. (2002). Simultaneous computation of gravity and magnetic anomalies resulting from a 2-D object. *Geophysics*, 67(3), 801-806.

Sniieder, R., & Trampert, J. (1999). Inverse problems in geophysics. In *Wavefield inversion* (pp. 119-190). Springer, Vienna.

Stocco, S., Godio, A., & Sambuelli, L. (2009). Modelling and compact inversion of magnetic data: A Matlab code. *Computers & Geosciences*, 35(10), 2111-2118.

Talwani, M. (1965). Computation with the help of a digital computer of magnetic anomalies caused by bodies of arbitrary shape. *Geophysics*, 30(5), 797-817.

Tarantola, A. (2005). *Inverse problem theory and methods for model parameter estimation* (Vol. 89). siam.

Telford, W. M., Geldart, L. P., & Sheriff, R. E. (1990). *Applied geophysics* (Vol. 1). Cambridge university press.

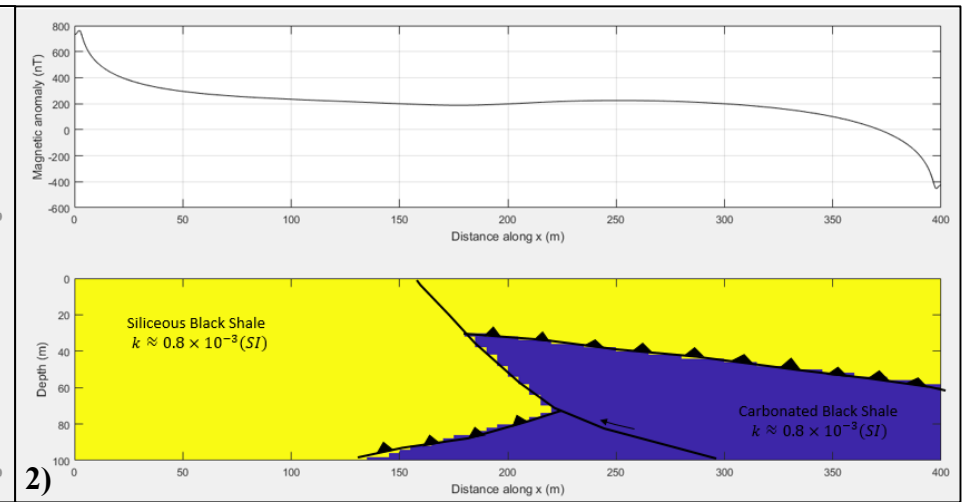
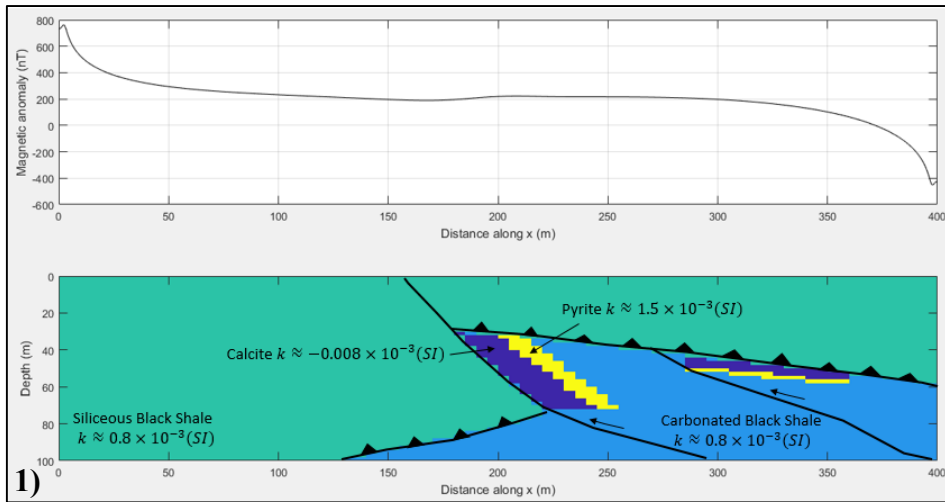
Vogel, C. R. (2002). *Computational methods for inverse problems* (Vol. 23). Siam.

Won, I. J., & Bevis, M. (1987). Computing the gravitational and magnetic anomalies due to a polygon: Algorithms and Fortran subroutines. *Geophysics*, 52(2), 232-238.

# Appendix A

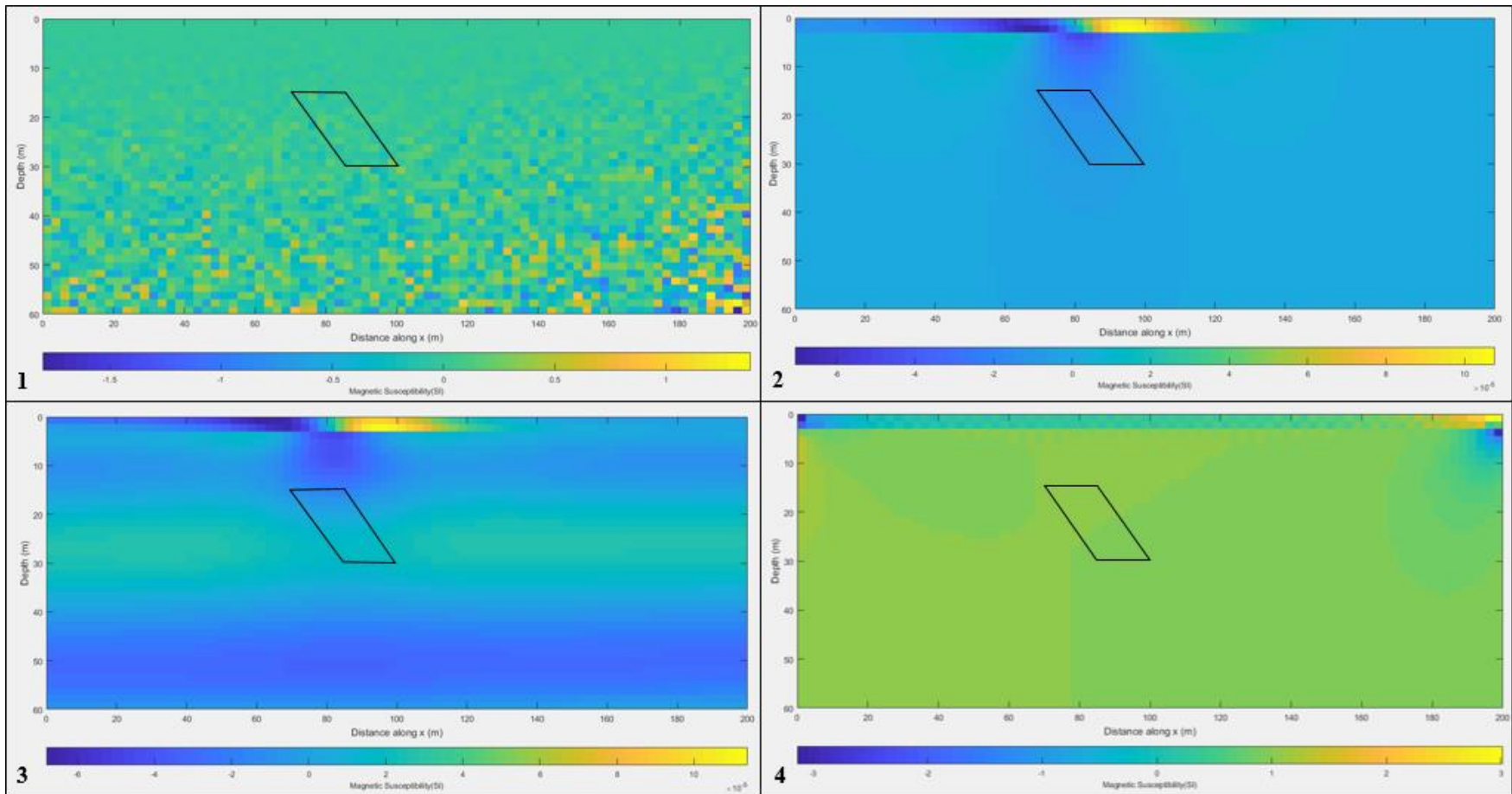
Comparison of the shape of the magnetic anomaly of the proposed synthetic model and the magnetic anomaly of the background. In the text it is presented the result of removing the magnetic properties of the background to the synthetic model which at the end is equivalent to only take into account the contrast of magnetic susceptibilities.

1) Model of the mineralization of the zone. The top of the biggest breccia is at 30 m and is dipping with an angle of  $45^\circ$ . The inclination of the geomagnetic field is  $I_0 = 29.2142^\circ$ . 2) Description of the background represented by a Siliceous Black Shale and a Carbonated Black Shale.



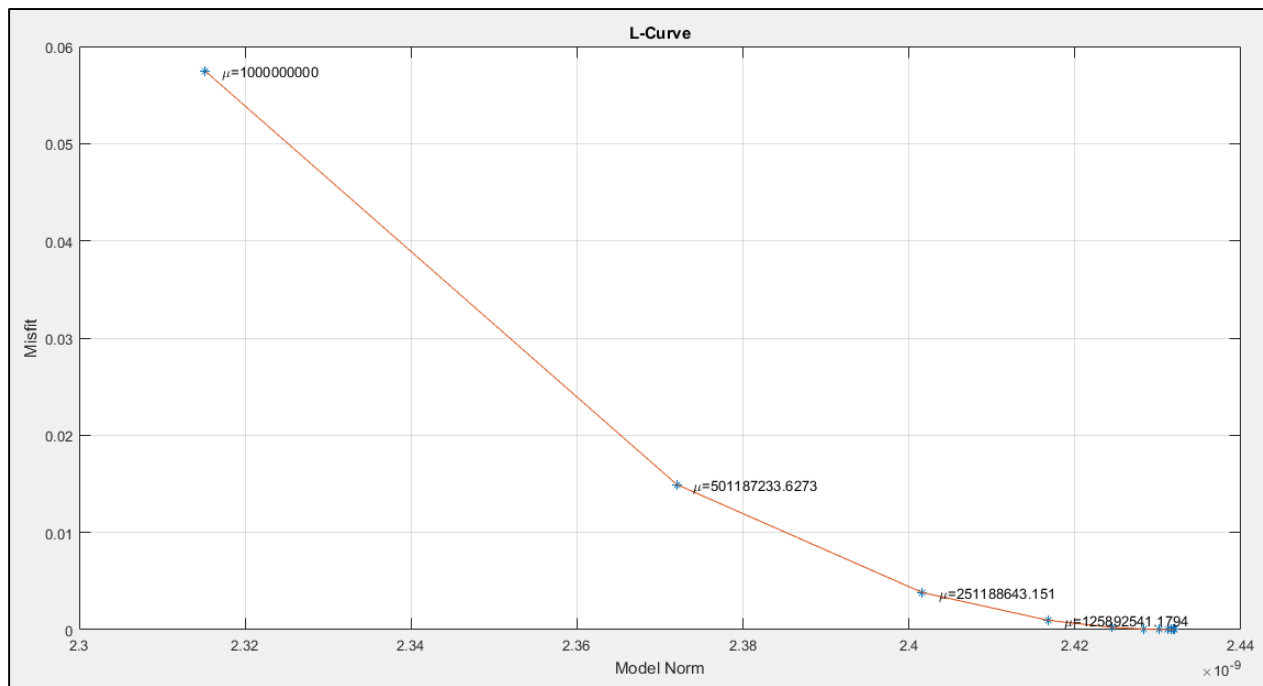
## Appendix B

Results of the inversion of the synthetic data with **1)** simple least squares, **2)** damped least squares, **3)** weighted damped least squares (with a matrix of first order derivatives) and **4)** Conjugate gradient (with 147 iterations and a tolerance of  $1 \times 10^{-20} nT$  of error). The contour demark the shape of the proposed body.



## Appendix C

1) Method of the L-curve to choose the best trade-off parameter to use in the damped least squares and weighted damped least squares methods for the inversion of the observed data. The value was of  $2.5119 \times 10^8$ .



## Appendix D

Inversion of 1) the profile 1 and 2) the profile 2 without the effect of the topography. If this figures are compared with figures 17 and 18 respectively, it is evident that the variations are minimal, being these only a small decrease in the contrast of magnetic susceptibilities. Magnetic susceptibility contrast ( $\Delta\chi_m$ ) is expressed in  $10^{-5}$  CGS system.

